GENE THERAPY

Kbtbd13 knockdown restores muscle function in a clinically relevant mouse model of nemaline myopathy type 6

Ricardo A. Galli[1,2]†‡*, Leander A. Vonk[1]‡, Rianne J. Baelde[1]‡, Anita van den Heuvel[3], Sylvia Bogaards[1], Stefan Conijn[1], Emma Siteur[1], Olga Alekhina[4], Henk Granzier[4], Thomas Irving[5,6], Weikang Ma[5,6,7], Karlijn Bouman[8], Baziel van Engelen[8], Silvère M. van der Maarel[3], Tyler J. Kirby[1,9,10,11], Nicol Voermans[8], Josine de Winter[1,9], Coen A.C. Ottenheijm[1,4,10]*

Nemaline myopathy type 6 (NEM6) is a rare neuromuscular disorder caused by pathogenic variants in the *Kelch repeat and BTB domain–containing 13* (*KBTBD13*) gene. Patients experience muscle weakness, excessive fatigue, and impaired muscle relaxation that affect their daily activities related to abnormal protein aggregation in muscle cells and a predominance of slow-twitch myofibers, and no specific therapies are available. Here, we studied a clinically relevant *Kbtbd13*:p.Arg408Cys knockin mouse model to elucidate the molecular changes driving disease pathogenesis through measurements of muscle contractility, single myofiber assays, super-resolution microscopy, and x-ray diffraction. *Kbtbd13*:p.Arg408Cys knockin mice closely phenocopied human NEM6 pathology at the morphological, functional, and transcriptional levels, with the p.Arg408Cys variant causing mislocalization of KBTBD13 in the muscle sarcomere, associated with disease onset between 1 and 3 months of age, plateauing by 9 months, and with little progression at 18 months. As a potential therapeutic approach, we knocked down *Kbtbd13* using short hairpin RNA against *Kbtbd13* delivered intramuscularly via an adeno-associated virus 9 vector at either the prephenotype (1-month-old) or peak-phenotype (3- or 7-month-old) stages. A single treatment at the prephenotype stage prevented the development of impaired relaxation kinetics, nemaline rod aggregation, and slow-twitch myofiber predominance at 3 months of age. A single treatment at 3 months of age, after onset of disease, restored muscle morphology, contractility, and muscle-relaxation kinetics over 6 months. These data provide insights into NEM6 pathogenesis and suggest that *Kbtbd13* knockdown might be a promising therapeutic strategy for patients with NEM6.

INTRODUCTION

Nemaline myopathies (NMs) constitute a large group of heterogeneous diseases with a constantly growing phenotypic spectrum, with a prevalence of 0.2:100,000 individuals (*1*). NMs are among the most common forms of nondystrophic congenital myopathies (*2*) and are characterized by extremity weakness and hypotonia (*3*). The onset, clinical presentation, and histopathological hallmarks are highly heterogeneous (*4*–*6*); however, common features include muscle weakness, aberrant protein aggregation (nemaline rods), slow-twitch myofiber predominance, and myofibrillar disarray (*7*–*9*). NM severity ranges from a nonprogressive or mild form to a fatal presentation, typically in early NM onset (*10*–*13*). To date, pathogenic variants in 13 genes encoding thin-filament proteins or proteins involved in sarcomere assembly have been identified to cause NM (*14*–*27*). Variants in the *Kelch repeat and BTB domain–containing 13* (*KBTBD13*) gene cause NM type 6 (NEM6) (*19*), and most patients carry the Dutch founder variant in KBTBD13 (NP_001094832.1: p.Arg408Cys), which results in a gain-of-function phenotype. *KBTBD13* is exclusively expressed in skeletal and cardiac muscle (*28*). Although its function has remained elusive, recent work suggests that it is an actin-binding protein that regulates thin-filament stiffness (*29*) and functions as a muscle-specific ubiquitin ligase (*30*). The NP_001094832.1 p.Arg408Cys missense variant is the most common. Patients with NEM6 present with impaired muscle relaxation kinetics (*31*–*34*), proximal and axial muscle weakness, increased muscle fatigue (*34*), and in some cases, respiratory (*19*) and cardiac dysfunction (*35*). Histopathologically, NEM6 muscle is characterized by accumulation of nemaline rods, cores, ragged-red myofibers, nuclear clumps, granulo-filamentous material, slow-twitch type I myofiber predominance and hypertrophy, and atrophy of fast-twitch type IIa myofibers (*9*, *19*, *33*, *36*–*38*). Although the clinical and histopathological phenotype of NEM6 overlaps with other congenital myopathies, one characteristic feature of NEM6 is the impaired muscle relaxation kinetics that adversely affect daily life activities (*34*) because patients present with muscle slowness, difficulty with running, and severe muscle fatigue. In vitro studies, performed on slow- and fast-twitch myofibers and myofibrils from patients with NEM6 and on a NEM6 mouse model (*29*), showed that the impaired muscle relaxation has a sarcomeric origin. However, no natural history data are available, complicating clinical prognosis and the timing of potential therapeutic interventions, should any become available. To

[1]Department of Physiology, Amsterdam UMC, Location VUMC, 1081HV Amsterdam, Netherlands. [2]Musculoskeletal Health, Amsterdam Movement Sciences, 1081HV Amsterdam, Netherlands. [3]Department of Human Genetics, Leiden University Medical Center, 2333ZC Leiden, Netherlands. [4]Department of Cellular and Molecular Medicine, University of Arizona, Tucson, AZ 85724, USA. [5]BioCAT, Department of Biology, Illinois Institute of Technology, Chicago, IL 60616, USA. [6]Center for Synchrotron Radiation Research and Instrumentation, Illinois Institute of Technology, Chicago, IL 60616, USA. [7]Pritzker Institute of Biomedical Science and Engineering, Illinois Institute of Technology, Chicago, IL 60616, USA. [8]Department of Neurology, Donders Institute for Brain, Cognition, and Behaviour, Radboud University Medical Center, 6525EN Nijmegen, Netherlands. [9]Tissue Function & Regeneration, Amsterdam Movement Sciences, 1081HV Amsterdam, Netherlands. [10]Heart Failure & Arrhythmias, Amsterdam Cardiovascular Sciences, 1081HV Amsterdam, Netherlands. [11]Division of Cardiovascular Medicine, Department of Internal Medicine, University of Kentucky, Lexington, KY 40536, USA.
†Present address: Neurogenetics Branch, National Institute of Neurological Disorders and Stroke, National Institutes of Health, Bethesda, MD 20814, USA.
‡These authors contributed equally to this work.
*Corresponding author. Email: Ricardo.galli@nih.gov (R.A.G.); c.ottenheijm@amsterdamumc.nl (C.A.C.O.)

address some of these issues, here, we (i) characterized the molecular changes induced by the *Kbtbd13*:p.Arg^{408}→Cys variant in a knockin mouse model [hereafter referred to as *Kbtbd13*(R408C)] and compared them with human pathology, (ii) established the natural history of NEM6 in *Kbtbd13*(R408C) mice to identify a therapeutic window, and (iii) evaluated the efficacy of *Kbtbd13* knockdown as a potential therapeutic intervention.

RESULTS

Characterization of human NEM6 skeletal muscle biopsies shows nemaline rod aggregates and slow-twitch type I myofiber predominance

We first characterized the morphological parameters of quadriceps muscle biopsies from individuals affected by NEM6 (patient demographics are in Table 1). In line with previous reports (*19*, *36*), single myofiber analysis of muscle cryosections from patients with NEM6 stained for adenosine triphosphatase (ATPase) showed a predominance of slow-twitch type I myofibers in individuals affected by NEM6 (Fig. 1A), and the myofiber-type shift did not correlate with age (Fig. 1, B and C). Representative Gömöri trichrome and ATPase staining for myosin heavy chain (MHC) quantification of NEM6 and control biopsies are shown in Fig. 1D. Although we did not observe a difference in the average cross-sectional area (CSA) of either slow- or fast-twitch myofibers between NEM6 and control samples (Fig. 1E), we observed an increase in the number of large slow-twitch type I myofibers in patients with NEM6 (Fig. 1F) and an increase in the number of small-sized type II myofibers compared with controls (Fig. 1G). Last, quantification of nemaline rods showed that about 50% of the NEM6 myofibers contained nemaline rods (Fig. 1H), with no correlation with age (Fig. 1I). Thus, myofiber type I predominance, increased myofiber size, and nemaline rods are hallmark features of NEM6; however, the natural history of these features in patients is unknown.

Kbtbd13(R408C) mice recapitulate the myofiber trophic changes observed in muscle biopsies of patients with NEM6

To unravel the natural history of the disease, we established a *Kbtbd13*(R408C) mouse model by knocking in the gene variant using CRISPR guide RNAs, as established previously (*39*). We then performed a longitudinal study to characterize muscle morphological and functional changes in 1-, 3-, 9-, and 18-month-old wild-type (WT) and *Kbtbd13*(R408C) male mice (Fig. 1A). First, we assessed whether *Kbtbd13*(R408C) recapitulated histopathological changes observed in human NEM6 muscle. Because muscles of patients with NEM6 were characterized by a predominance of slow-twitch type I myofibers, we assessed the myofiber-type composition in whole muscles of WT and *Kbtbd13*(R408C) mice, finding that myofiber-type

Table 1. Demographic and muscle biopsy assay information for patients with NEM6 and healthy controls. ATPase, myosin heavy chain determination by ATP pH staining; GT, Gömöri trichrome; fts-RNA-seq, fiber type–specific RNA sequencing; QUA, quadriceps muscle; N/A, not applicable; ✓, the listed assay was performed for that biopsy. An empty cell indicates that the listed assay was not performed.

ID	Sex	Variant	Muscle biopsied	Age at biopsy	ATPase	GT	CSA	fts-RNA-seq
NEM6_1	F	c.1222C>T (p.(Arg408Cys))	QUA	16	✓	✓	✓	
NEM6_2	F	c.1222C>T (p.(Arg408Cys))	QUA	18	✓	✓		
NEM6_3	F	c.1222C>T (p.(Arg408Cys))	QUA	28	✓	✓		✓
NEM6_4	M	c.1222C>T (p.(Arg408Cys))	QUA	30	✓	✓		✓
NEM6_5	F	c.1222C>T (p.(Arg408Cys))	QUA	33	✓	✓		✓
NEM6_6	F	c.1222C>T (p.(Arg408Cys))	QUA	42	✓	✓	✓	
NEM6_7	F	c.1222C>T (p.(Arg408Cys))	QUA	43	✓	✓		
NEM6_8	F	c.1222C>T (p.(Arg408Cys))	QUA	45	✓	✓	✓	
NEM6_9	F	c.1222C>T (p.(Arg408Cys))	QUA	56	✓	✓		
NEM6_10	M	c.1222C>T (p.(Arg408Cys))	QUA	67		✓		
NEM6_11	F	c.1222C>T (p.(Arg408Cys))	QUA	34	✓	✓	✓	
NEM6_12	M	c.1222C>T (p.(Arg408Cys))	QUA	62		✓	✓	
Control_1	M	N/A	QUA	45	✓	N/A	✓	
Control_2	M	N/A	QUA	50	✓	N/A	✓	
Control_3	M	N/A	QUA	50	✓	N/A	✓	
Control_4	F	N/A	QUA	65	✓	N/A	✓	
Control_5	F	N/A	QUA	52	✓	N/A	✓	✓
Control_6	F	N/A	QUA	53	✓	N/A	✓	
Control_7	F	N/A	QUA	51	✓	N/A	✓	
Control_8	F	N/A	QUA	62	✓	N/A	✓	✓
Control_9	M	N/A	QUA	57	✓	N/A	✓	✓
Control_10	F	N/A	QUA	51	✓	N/A	✓	
Control_11	M	N/A	QUA	58	✓	N/A	✓	
Control_12	M	N/A	QUA	53	✓	N/A	✓	

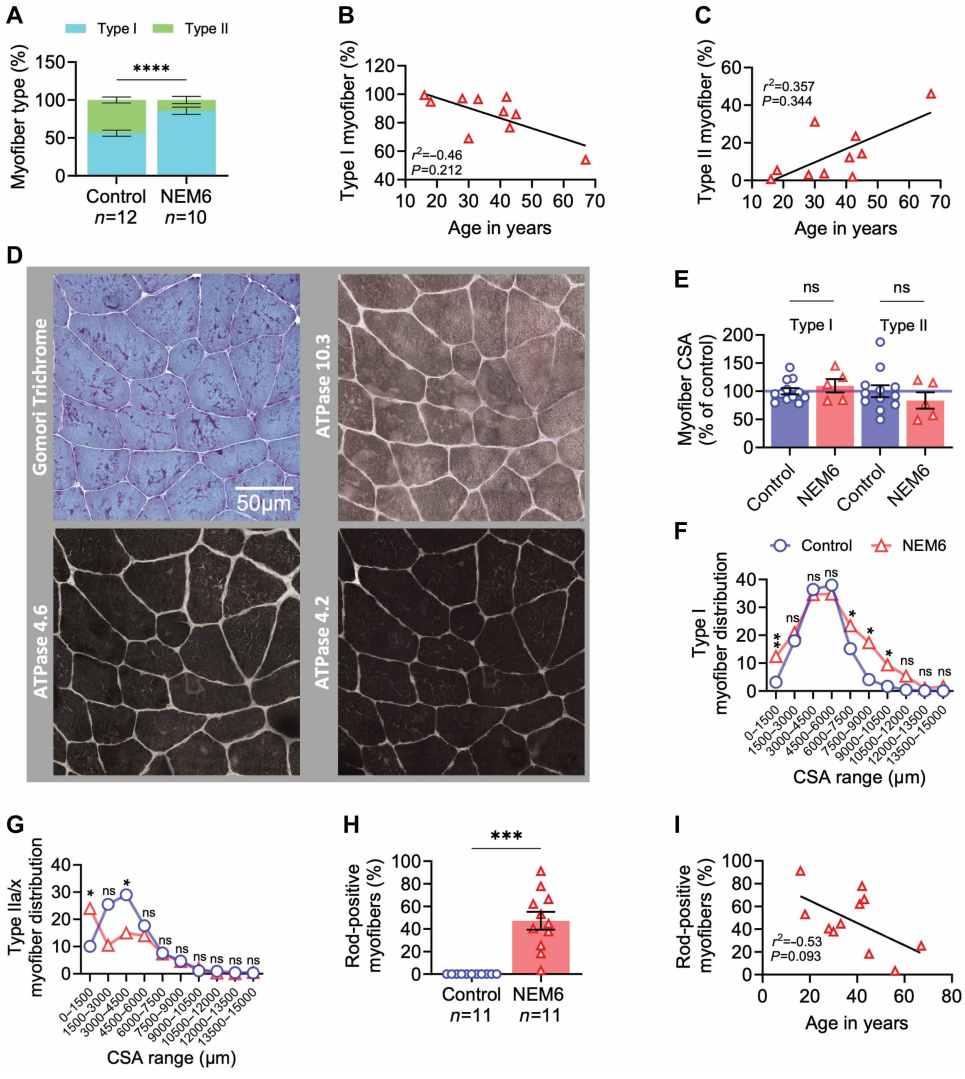

Fig. 1. Morphological characterization of human NEM6 quadriceps muscle biopsies. (**A**) Type I and type II myofiber distribution in biopsy samples from healthy controls and patients with NEM6 ($n = 12$ and $n = 10$, respectively), as assessed by muscle fiber–type staining. (**B**) Correlation between NEM6 slow-twitch type I myofiber type and age ($n = 10$). (**C**) Correlation between NEM6 fast-twitch type II myofiber type and age ($n = 10$). (**D**) Representative images of muscle cross sections from patients with NEM6, stained for Gömöri trichrome to visualize nemaline rods (top left), ATPase 10.3 to visualize fast myosin heavy chains (top right), and ATPase 4.6 (bottom left) and ATPase 4.2 (bottom right), both for slow myosin heavy chain determination. Scale bars, 50 µm. (**E**) Single myofiber CSA analysis (NEM6: $n = 5$; controls: $n = 12$). (**F**) Slow-twitch type I myofiber CSA distribution. (**G**) Fast-twitch type II myofiber CSA distribution. (**H**) Muscle biopsy nemaline rod quantification. (**I**) Correlation between nemaline rod and age (NEM6: $n = 11$). Statistical analysis: For data in (A), a two-way ANOVA with uncorrected Fisher's least significant difference was used. For data in (B), (C), and (I), a Spearman rank test was used to investigate correlations. For data in (E) and (H), an unpaired t test with Welch's correction was used. For data in (F) and (G), a multiple unpaired t test corrected for multiple comparisons using false discovery rate (FDR) was used. Significance was set to $P < 0.05$ (*$P < 0.05$, **$P < 0.01$, ***$P < 0.001$, and ****$P < 0.0001$), and all data are presented as the means ± SEM. ns, not significant.

distribution in the whole soleus muscles of *Kbtbd13*(R408C) mice was comparable to that of WT mice at 1 month of age; however, from 3 months of age onward, we observed a shift toward a predominant slow-twitch type I myofiber phenotype. The phenotype peaked at 9 months and remained stable onward (Fig. 2B, left and middle panels). The extensor digitorum longus (EDL) muscle showed a shift in myofiber type, characterized by a progressive loss of fast-twitch type IIb myofibers at 3, 9, and 18 months, with an increase in fast-twitch type IIx myofibers at 9 months. Note that at all ages, the EDL muscles of *Kbtbd13*(R408C) mice showed an increasing number of slow-twitch type I myofibers, whereas in the WT muscles, no slow-twitch type I myofibers were observed (Fig. 2B, right panel). The diaphragm, quadriceps, gastrocnemius, and tibialis anterior muscles (fig. S1A) also showed a myofiber-type transition with a shift toward a more oxidative myofiber phenotype. Like myofibers in biopsies of patients with NEM6, *Kbtbd13*(R408C) muscles demonstrated hypertrophy of slow-twitch type I myofibers and fast-twitch type IIa myofibers in soleus muscle, starting at 3 months onward (Fig. 2C). In contrast with soleus muscle, in EDL muscle, fast-twitch type IIa and IIx myofibers were atrophied at most ages (Fig. 2D). CSA analyses in the diaphragm, quadriceps, gastrocnemius, and tibialis anterior muscles also showed muscle-specific changes that were milder than in the soleus and EDL (fig. S1B). Soleus myofiber CSA distribution analyses at 1, 3, 9, and 18 months of age are shown in fig. S1C.

We next studied nemaline rod accumulation in *Kbtbd13*(R408C) muscles. Although no nemaline rods were observed in slow-twitch soleus and fast-twitch EDL muscles from 1-month-old mice, at 3, 9, and 18 months, nemaline rod accumulation was evident, peaking at 9 months and with little progression at 18 months (Fig. 2E). Nemaline rod accumulation was observed across all studied muscles, including diaphragm, quadriceps, gastrocnemius, and tibialis anterior muscles, although to a much lesser extent than compared with soleus and EDL muscles (fig. S1, D and E). Because the morphological data suggested a myofiber type–dependent phenotype, where slow-twitch soleus muscle was more affected, we analyzed the myofiber type–dependent accumulation of nemaline rods in soleus and EDL myofibers to determine whether there is a myofiber type–dependent phenotype in 3- and 9-month-old muscles, because these ages represented the onset and peak phenotypes, respectively. In the soleus muscle, fast-twitch type IIa myofibers showed a higher amount of nemaline rods than slow-twitch type I myofibers at 3 months, but this was no longer observed at 9 months (Fig. 2F), possibly because

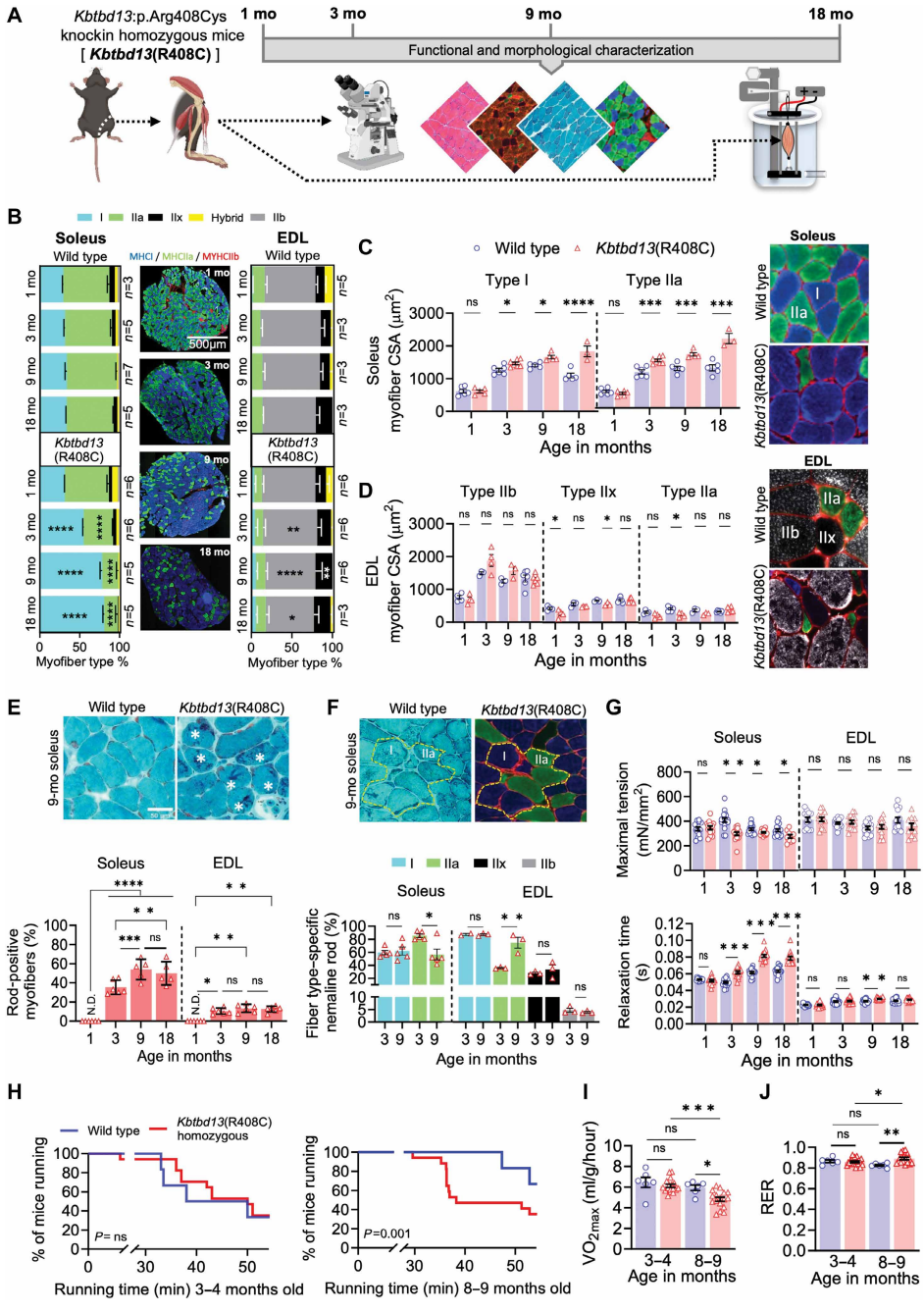

Fig. 2. *Kbtbd13*(R408C) mouse model morphological and functional characterization. (**A**) Schematic representation of the morphological and functional pipeline for skeletal muscle characterization in the *Kbtbd13*:p.Arg408Cys knockin homozygous male mouse model [*Kbtbd13*(R408C)]. Schematic figure created in part with BioRender.com. (**B**) Left panel: Whole soleus muscle myofiber-type distributions over time in WT and *Kbtbd13*(R408C) mice. Middle panel insets: Representative images of whole soleus muscle myofiber-type compositions in *Kbtbd13*(R408C) mice at different ages. Right panel: Whole EDL muscle myofiber-type distributions over time in WT and *Kbtbd13*(R408C) mice. (**C**) Soleus myofiber type–specific CSA. The right panel shows representative images of the soleus muscle cross section stained for different myosin heavy chains. (**D**) EDL myofiber type–specific CSA. The right panel shows representative images of EDL muscle cross sections stained for different myosin heavy chains. (**E**) The top panel shows representative images of soleus muscle cross sections from 9-month-old WT (left) and *Kbtbd13*(R408C) mice (right) stained with modified Gömöri trichrome for nemaline rod visualization (white asterisks indicate nemaline rods). The bottom panel shows nemaline rod quantification in soleus and EDL muscle over time (N.D., not detectable). For soleus muscle, $n = 6$ mice per genotype at 1 and 3 months and $n = 5$ mice per genotype at 9 and 18 months. For EDL analyses, $n = 6$ mice per genotype at all ages. (**F**) The top panel shows representative serial muscle sections stained with modified Gömöri trichrome for nemaline rod visualization (left) and with immunolabeling for myosin heavy chain visualization (right). The areas highlighted in yellow are the same region in serial sections. The bottom panel shows myofiber type–specific nemaline rod quantification in soleus and EDL muscles in 3- and 9-month-old male *Kbtbd13*(R408C) mice. For soleus muscle, $n = 5$ mice at 3 and 9 months of age, and for EDL analyses, $n = 3$ at 3 and 9 months of age. Muscle myofiber types are color coded. Cyan: I; green: IIa; black: IIx; gray: IIb. (**G**) Top panel: In vitro whole soleus and EDL maximal tensions in WT and *Kbtbd13*(R408C) mice at 1, 3, 9, and 18 months of age. Bottom panel: In vitro whole soleus and EDL relaxation times in WT and *Kbtbd13*(R408C) mice at 1, 3, 9, and 18 months of age. (**H**) Left and right panels: Survival plot for time running on a treadmill to analyze fatigability in WT and *Kbtbd13*(R408C) mice at 3 to 4 and 8 to 9 months of age, respectively. (**I**) VO_{2max} consumption to analyze respiratory capacity during the treadmill running protocol in WT and *Kbtbd13*(R408C) mice at 3 to 4 and 8 to 9 months of age, respectively. (**J**) Respiratory exchange ratio (RER) during the treadmill running protocol to analyze the metabolic state in WT and *Kbtbd13*(R408C) mice at 3 to 4 and 8 to 9 months of age, respectively. Statistical analysis: Two-way ANOVA with Šidák's multiple comparison test was performed for (B) to (E), (G), (I), and (J). Unpaired *t* tests were performed for data in (F). A log-rank test (Mantel-Cox test) was performed to compare the survival curves in (H): Genotypes were compared within age groups, and the same genotypes were compared at different ages to determine time-dependent changes. A restricted mean survival time analysis (RMST) with tau set at 55 min was used to calculate the area under the curve (AUC) for calculating the average running time per genotype. Significance was set to $P < 0.05$ (*$P < 0.05$, **$P < 0.01$, ***$P < 0.001$, and ****$P < 0.0001$), and all data are presented as the means ± SEM.

of the progressive loss of fast-twitch type IIa myofibers (Fig. 2B). In EDL muscle, fast-twitch type IIa myofibers showed fewer nemaline rods as compared with slow-twitch type I myofibers at 3 months, opposite to what was observed in soleus muscle. In addition, fast-twitch type IIa myofibers were more affected at 9 months compared with 3 months (Fig. 2F), possibly reflecting the slight increase in the number of fast-twitch type IIa myofibers observed in EDL. Furthermore, we characterized *Kbtbd13* expression (fig. S1F) along with the expression of main sarcomeric genes involved in NM (fig. S1G) at different ages and showed a time-dependent effect of the *Kbtbd13*(R408C) variant.

Functionally, patients with NEM6 present with mild muscle weakness accompanied by slow muscle relaxation kinetics, which is not reported in other NMs and is the main complaint of individuals

who are affected. Therefore, we characterized the contractile parameters of slow-twitch soleus and fast-twitch EDL muscles of male *Kbtbd13*(R408C) and WT mice. At 1 month of age, soleus maximal active tension (maximal force normalized to CSA) and relaxation kinetics were comparable to those of WT mice. However, as with the morphological changes, maximal tension and relaxation kinetics were affected at 3, 9, and 18 months in *Kbtbd13*(R408C) mice compared with WT controls. EDL muscles displayed no changes in maximal active tension but an impairment in relaxation kinetics at 9 months (Fig. 2G, top and bottom panels), suggesting a milder phenotype. Female *Kbtbd13*(R408C) mice were also assessed and showed similar changes: Soleus muscles had increased muscle mass and hypertrophy of slow-twitch type I and fast-twitch type IIa myofibers, in line with a shift toward an oxidative phenotype, presented also with nemaline rod accumulation and impaired muscle relaxation kinetics (fig. S2, A to F).

Last, because patients with NEM6 are characterized by increased fatigability (*34*), we studied whether the observed contractile changes impaired global physical performance in *Kbtbd13*(R408C) mice. First, we tested the endurance capacities of WT versus *Kbtbd13*(R408C) male mice during a treadmill running protocol. We observed no differences in median running time in 3- to 4-month-old mice, although a difference was observed at 8 to 9 months, the age at which the morphological phenotype peaks (Fig. 2H, left and right panels). VO_{2max}, the maximum amount of oxygen used during exercise, was also reduced in 8- to 9-month-old *Kbtbd13*(R408C) mice compared with WT mice (Fig. 2I), suggesting that *Kbtbd13*(R408C) mice have lower endurance capacity. The respiratory exchange ratio at VO_{2max} was increased in *Kbtbd13*(R408C) mice at this age, suggesting a shift in fuel-type consumption, favoring the glycolytic system (Fig. 2J). These data support the notion that *Kbtbd13*(R408C) mice closely phenocopy the morphological and functional phenotypes of patients with NEM6, including a shift toward an oxidative phenotype, nemaline rod accumulation, contractile weakness, impaired muscle relaxation kinetics, and increased fatigability, manifesting between 1 and 3 months and peaking at 9 months.

KBTBD13:p.Arg408Cys impairs protein localization in vitro and in vivo

Previous work has shown that KBTBD13 interacts with the actin filament, and mutant KBTBD13 alters the actin filament structure (*29*). A hallmark of biopsies of patients with NEM6 is nemaline rod aggregation, which is composed in part of actin (*40*, *41*). To study whether impaired actin protein dynamics cause the nemaline rod accumulation, we determined the rate of actin polymerization and depolymerization in the presence of recombinant WT or KBTBD13:p.Arg408Cys protein. We did not observe differences in the rate of actin polymerization or depolymerization between the WT and KBTBD13:p.Arg408Cys proteins (Fig. 3A), suggesting that actin dynamics do not play a role in nemaline rod formation in NEM6. Next, we investigated the localization of KBTBD13 in the sarcomere. We conditionally overexpressed KBTBD13 WT or KBTBD13:p.Arg408Cys protein fused with the mNeonGreen fluorescent reporter in C2C12 mature myotubes using a doxycycline-inducible system. Note that the mNeonGreen tag was fused to the N terminus of KBTBD13 to avoid interference with the Kelch domains. Overexpression of WT KBTBD13 showed a striation pattern that localized to the thin filaments, flanking the Z-disk (Fig. 3B, top panel), whereas in the p.Arg408Cys variant, the striation pattern for the KBTBD13 signal was lost, and KBTBD13:p.Arg408Cys appeared to randomly aggregate to different sarcomeric structures (Fig. 3B, bottom panel). Mock mNeonGreen-expressing myotubes are shown in fig. S3A. Because we observed a different localization pattern between WT and mutant KBTBD13 in C2C12 cells, we next tested whether KBTBD13 also localizes to the sarcomere's thin filaments in a previously developed *Kbtbd13* knockout (KO) mouse model, which lacks endogenous *Kbtbd13* expression (*39*). We treated the mouse soleus muscles with an intramuscular injection of an adeno-associated virus serotype 9 (AAV9) encoding either the KBTBD13 WT or p.Arg408Cys (KBTBD13 R408C) protein, fused to an enhanced green fluorescent protein (eGFP) reporter (Fig. 3C). We observed up-regulation of *eGfp* and *Kbtbd13* transcripts compared with untreated WT and *Kbtbd13* KO muscles (Fig. 3D). In KBTBD13(R408C)-treated muscles, *eGfp* and *Kbtbd13* transcripts were both 5.26 times higher than in KBTBD13(WT)-treated muscles (Fig. 3D). We confirmed protein expression by measuring KBTBD13 eGFP signal intensity in longitudinal soleus muscle sections of KBTBD13(R408C)- and KBTBD13(WT)-treated mice (Fig. 3E). To analyze the localization of KBTBD13(WT) and KBTBD13(R408C) protein, we isolated single myofibers from treated soleus muscles and performed super-resolution imaging. KBTBD13(WT) protein flanked the Z-disk and localized to the thin filaments (Fig. 3F, top panel), similar to the C2C12 myotube localization data. However, in KBTBD13(R408C)-expressing myofibers, thin-filament localization was lost, with predominant localization to the Z-disk and other sarcomere structures in an aggregated pattern (Fig. 3F, middle panel). To rule out the idea that the overexpressed protein was accumulating in the less protein-dense I-band region of the sarcomere, we analyzed the width of the KBTBD13 WT eGFP signal intensity relative to α-actinin (Z-disk marker) at incremental sarcomere lengths, which revealed an about 190-nm increase in eGFP signal width per micrometer of lengthening (Fig. 3G), which is consistent with thin-filament extension and much less than I-band extension (500 nm/μm) (*42*). Altogether, these data suggested that KBTBD13 localized to the thin filament and that the p.Arg408Cys variant altered its sarcomeric localization.

Kbtbd13(R408C) induces muscle-specific nanostructural changes in the muscle thin filament

To further investigate the contribution of KBTBD13(R408C) to thin-filament stiffness, we investigated thin-filament nanostructural changes through small-angle x-ray diffraction in slow-twitch soleus and fast-twitch EDL muscles from 9-month-old male mice, the age at which morphological and functional pathophysiological changes peak (Fig. 4A). Briefly, isolated soleus and EDL muscles from 9-month-old male WT and *Kbtbd13*(R408C) mice were excised and electrically stimulated ex vivo, and low-angle x-ray diffraction patterns were obtained in relaxed and maximally activated states, allowing us to obtain high-quality equatorial and meridional diffraction patterns of thin filaments. In soleus muscle, the actin layer line 6 (ALL6) reflection, which indicates the left-handed pitch of the thin-filament helix, and the 2.7-nm reflection, which indicates actin subunit spacing, were reduced in both the relaxed and activated states in *Kbtbd13*(R408C) mice (Fig. 4, B and C, left panels). The change in actin spacing (Δ2.7 nm) going from the relaxed to activated state was reduced in *Kbtbd13*(R408C) mice (Fig. 4C, right panel), suggesting that the thin filaments stretched less during activation. Next, we calculated thin-filament stiffness by

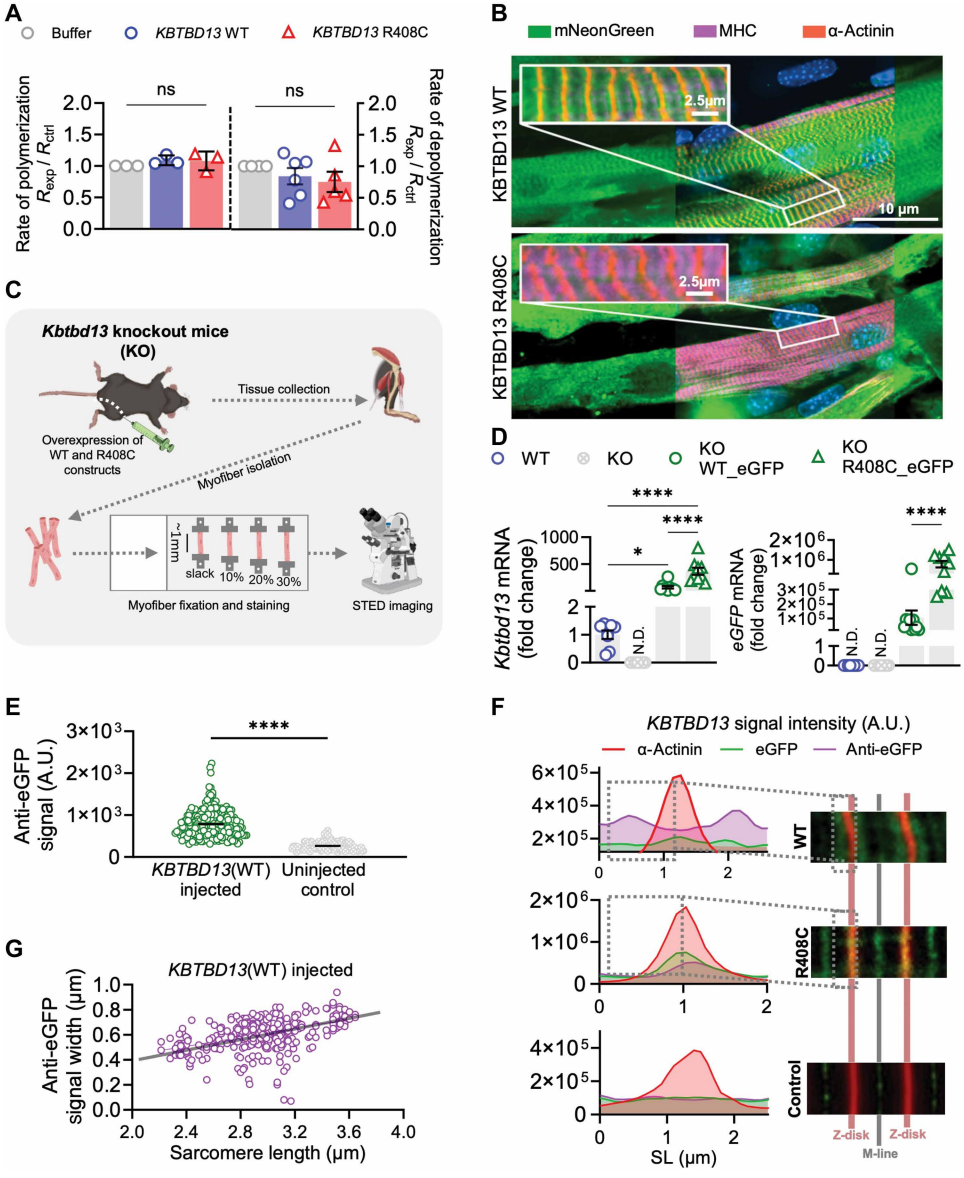

Fig. 3. Actin dynamics and KBTBD13 protein localization in the 9-month-old *Kbtbd13* KO mouse model. (**A**) Actin rate of polymerization and depolymerization. (**B**) Top and bottom panels: Representative images of in vitro KBTBD13 WT and R408C protein expression in C2C12 myotubes. (**C**) Schematic representation of the in vivo *KBTBD13* localization protocol. Created in part with BioRender.com. In brief, soleus muscles were injected with AAV9-expressing KBTBD13(WT)- or KBTBD13(R408C)-eGFP constructs. After 8 weeks, single myofibers were isolated and stretched at different sarcomere lengths and stained with anti-eGFP; STED imaging was performed. STED, stimulated emission depletion. (**D**) Relative *Kbtbd13* and *eGfp* mRNA normalized to the housekeeping gene *Rpl13a* in soleus muscles of untreated WT ($n = 4$), untreated *Kbtbd13* KO mice ($n = 4$), and KO mice injected with *KBTBD13*(WT) ($n = 4$) or *KBTBD13*(R408C) ($n = 4$) protein constructs tagged with eGFP. (**E**) *KBTBD13*(WT) eGFP signal intensity in injected soleus muscle longitudinal sections compared with contralateral uninjected soleus muscle. A.U., arbitrary units. (**F**) Signal intensity colocalization analysis in *Kbtbd13* KO soleus myofibers expressing *KBTBD13*(WT) (top panel) and *KBTBD13*(R408C) (middle panel) proteins. The bottom panel shows the signal intensity of the untreated control KO soleus muscle. SL, sarcomere length. (**G**) Anti-eGFP signal width changes relative to sarcomere length in *Kbtbd13* KO myofibers expressing *KBTBD13*(WT) protein. Statistical analysis: A one-way ANOVA was performed on the data in (A). A two-way ANOVA with Šidák's multiple comparison test was performed on the data in (D), and an unpaired *t* test was performed for the data in (E). Significance was set to $P < 0.05$ (*$P < 0.05$, **$P < 0.01$, ***$P < 0.001$, and ****$P < 0.0001$), and all data are presented as the means ± SEM. Each data point represents one mouse sample.

normalizing the force per thin filament to Δ2.7 nm, which revealed that thin-filament stiffness was higher in the soleus muscles of *Kbtbd13*(R408C) mice (Fig. 4D). Note that some of the data in Fig. 4 (A to D) have been previously published by us (*29*).

X-ray reflections of EDL muscle revealed that in contrast with the soleus muscles, EDL muscles of *Kbtbd13*(R408C) mice showed no difference in ALL6 spacing or in the 2.7-nm reflections in relaxed conditions, whereas during activation, these were increased (Fig. 4, E and F, left panel). However, Δ2.7 nm was comparable between *Kbtbd13*(R408C) and WT mice (Fig. 4F, right panel), and thin-filament stiffness was comparable between EDL muscles of WT and *Kbtbd13*(R408C) mice (Fig. 4G). Thus, these data suggested that the *Kbtbd13*:p.Arg408Cys variant induces muscle-specific thin-filament nanostructural changes and supported the notion that thin-filament stiffening contributes to slow relaxation muscle relaxation kinetics in a muscle type–dependent manner.

Kbtbd13(R408C)-induced transcriptional changes are myofiber type–dependent in mice and humans

Because the morphological and functional phenotype develops between 1 and 3 months, we next studied whether the onset of these phenotypes coincides with, or is preceded by, transcriptional changes in the soleus muscle, which would help determine the timing of potential therapy (Fig. 5A). Principal components analysis (PCA) plots of transcriptomic data from the soleus muscles of 1-month-old male *Kbtbd13*(R408C) mice are shown in fig. S4A. We identified only 56 differentially expressed genes (DEGs) in slow-twitch type I myofibers and 47 DEGs in fast-twitch type IIa myofibers (fig. S4B). Gene Ontology (GO) analysis showed no significant ($P > 0.05$) relevant biological processes (fig. S4C, left and right panels). We next analyzed the myofiber type–specific transcriptional profile at an overt-phenotype stage (3-month-old mice) and compared the data with human NEM6 myofiber type–specific changes. The PCA plot from

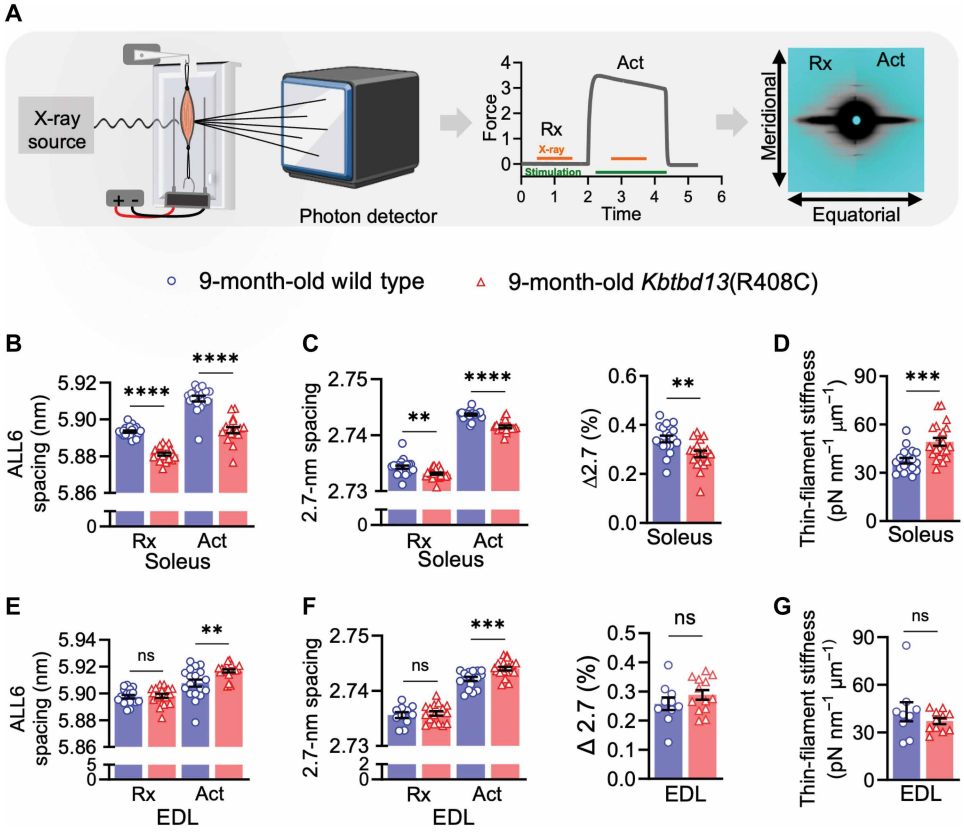

Fig. 4. Thin-filament nanostructural changes in WT and *Kbtbd13*(R408C) mouse soleus and EDL muscles. (**A**) Schematic representation of the small-angle x-ray diffraction protocol. WT and *Kbdbt13*(R408C) soleus muscles were exposed to a high-intensity x-ray beam, and diffraction patterns were collected with a photon detector. Samples were exposed to the x-ray beam during relaxed (Rx) and activated (Act) states. Images were collected, and equatorial and meridional reflections were analyzed. Created in part with BioRender.com. (**B**) Spacing of the ALL6 reflection during Rx and Act states in soleus muscles. (**C**) The left panel shows the actin subunit spacing (2.7 nm) during Rx and Act states in the soleus muscle. The right panel shows the change in the actin subunit spacing (Δ2.7 nm) during maximal tetanic activation. (**D**) Quantification of soleus muscle thin-filament stiffness. (**E**) Spacing of the ALL6 reflection during Rx and Act states in EDL muscles. (**F**) The left panel shows the actin subunit spacing (2.7 nm) during Rx and Act states in EDL muscles. The right panel shows the change in the actin subunit spacing (Δ2.7 nm) during maximal tetanic activation in EDL muscles. (**G**) Quantification of EDL muscle thin-filament stiffness. Statistics: A one-way ANOVA with Tukey's multiple comparison test was performed for data in (B), (C) (left panel), (E), and (F) (left panel). An unpaired *t* test was performed for the data in (C) (left panel), (D), (F) (left panel), and (G). Significance was set to $P < 0.05$ (**$P < 0.01$, ***$P < 0.001$, and ****$P < 0.0001$), and all data are presented as the means ± SEM.

3-month-old mice and biopsies of patients with NEM6 is shown in fig. S4 (D and E). A high number of DEGs in 3-month-old mice and human NEM6 slow-twitch type I and fast-twitch type IIa samples was identified (Fig. 5, B and C). To highlight the relevant biological processes represented by the DEGs, we performed GO analysis on the significant DEGs ($P < 0.05$). The main GO terms involved in 3-month-old slow-twitch type I *Kbtbd13*(R408C) myofibers showed increased proteotoxic/endoplasmic reticulum stress, reflected by increased ubiquitin-proteosome system and endoplasmic reticulum degradation–associated activity, coupled with activation of DNA damage/p53 activity and increased transforming growth factor–β signaling, which might reflect increased myofiber remodeling as observed in the natural history study (Fig. 5D, top panel). GO term analysis of *Kbtbd13*(R408C) mouse type IIa myofibers indicated changes in the regulation in lipid storage and regulation of metabolic processes (Fig. 5D, bottom panel), supporting the treadmill data that indicated that these mice undergo metabolic adaptations, as well as terms associated with myofibril assembly and sarcomere organization, consistent with the observed loss of type IIa myofibers. GO term analysis of myofibers from patients with NEM6 also revealed a myofiber type–dependent transcriptional profile (Fig. 5E, top and bottom panels). Unlike *Kbtbd13*(R408C) mouse type I myofibers, type I myofibers from patients with NEM6 were characterized by strong down-regulation in oxidative phosphorylation and electron transport chain pathways, possibly reflecting mitochondrial suppression and reduction in ATP (adenosine 5′-triphosphate) production. Human NEM6 type IIa myofibers also showed a myofiber type–specific phenotype reflected by an activated proteostasis and repair program, increased autophagy, and increased sarcomeric remodeling, which might reflect active changes occurring at a fiber-specific level. In Fig. 5F, a Venn diagram highlighting the GO terms that overlap between slow-twitch type I and fast-twitch type IIa myofibers of *Kbtbd13*(R408C) mice and patients with NEM6 is shown. Because there was low overlap of GO terms between the same myofiber types from *Kbtbd13*(R408C) mice and patients with NEM6, we further analyzed the intermyofiber transcriptional changes by comparing the number of overlapping GO terms between *Kbtbd13*(R408C) slow-twitch type I myofibers versus fast-twitch type IIa myofibers from patients with NEM6 and vice versa (table S3), which revealed a higher overlap in GO terms when comparing different myofiber types between mice and humans than when comparing the same myofiber types between species. This might be partially explained by evolutionary divergence, in which the same myofiber types in mice and humans might differ at the transcriptional level (*43*). To further explore a possible transcriptional similarity between mice and humans, we compared whole soleus RNA sequencing–based GO term overlap with human slow-twitch type I and fast-twitch type IIa myofibers because the soleus muscle expresses only myofiber types found in human muscle. This revealed a higher degree of overlap between whole soleus muscles from mice and human myofibers (table S4) than seen in the previous analysis. This finding is supported by previous work showing that soleus muscle transcriptionally phenocopies human quadriceps biopsies more closely than other mouse hindlimb muscles (*44*).

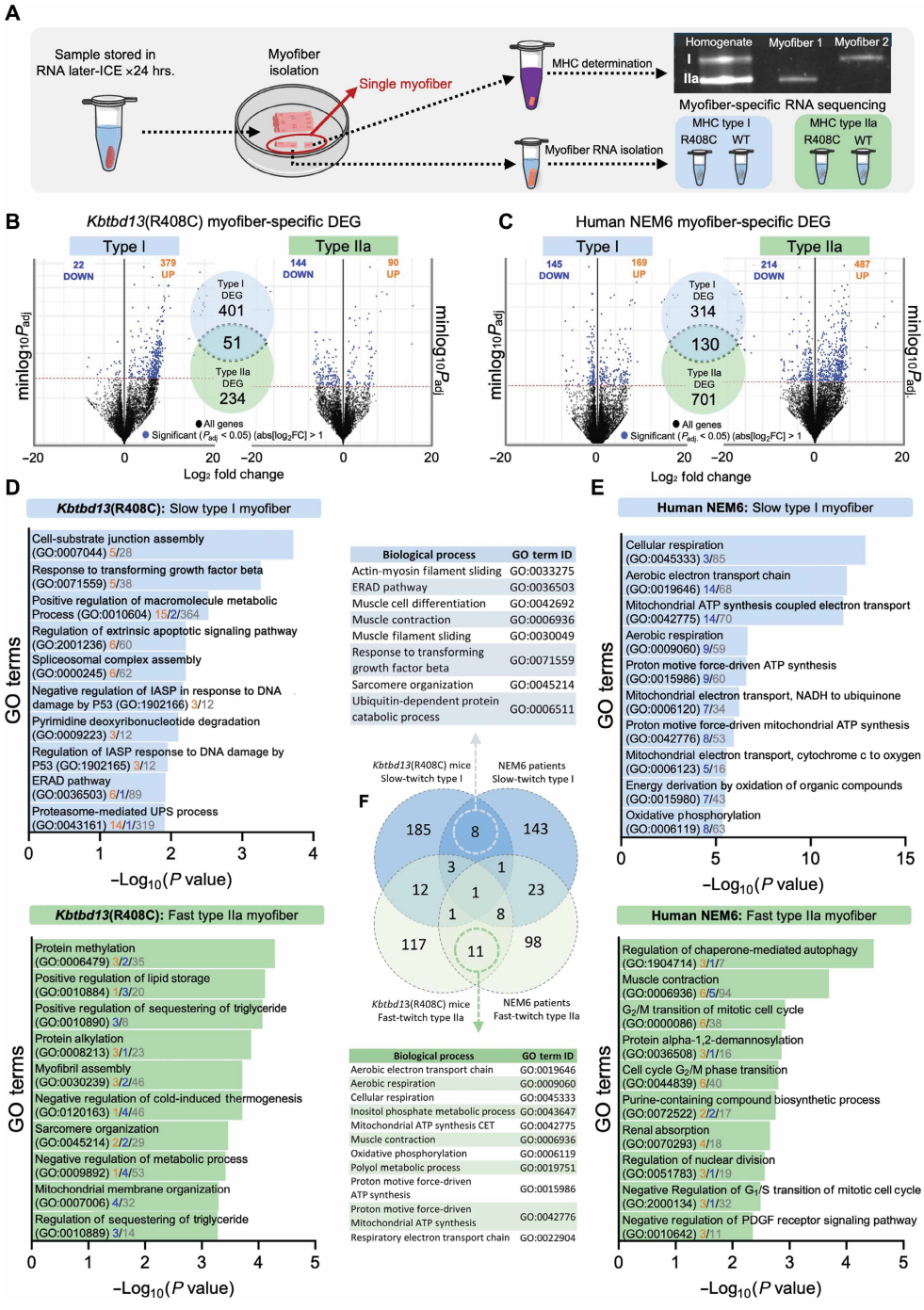

Fig. 5. *Kbtbd13*(R408C) mouse and human NEM6 myofiber type–specific transcriptional profiles. (**A**) Schematic representation of the pipeline to isolate single type I and type IIa mouse and human muscle myofibers for RNA sequencing based on their myosin heavy chain composition, as determined by SDS–polyacrylamide gel electrophoresis. Created in part with BioRender.com. (**B**) Volcano plot showing all DEGs for type I (left) and type IIa (right) myofibers from 3-month-old male mouse soleus muscles ($n = 4$ soleus muscles per genotype). A Venn diagram (middle) shows the type I and type IIa myofibers' significant DEGs, with the number of overlapping genes between myofiber types. (**C**) Volcano plot showing all DEGs for human NEM6 type I (left) and type IIa (right) myofibers ($n = 3$ muscle biopsies per individual). A Venn diagram (middle) shows the type I and type IIa myofibers' significant DEGs, with the number of overlapping genes between myofiber types. (**D**) Bar chart of the top 10 enriched biological processes for *Kbtbd13*(R408C) mouse soleus type I (top) and type IIa myofibers (bottom). (**E**) Bar chart of the top 10 enriched biological processes for human type I (top) and type IIa myofibers (bottom) from patients with NEM6. Note that the top 10 enriched terms for the input gene set are displayed on the basis of the $-\log_{10}(P$ value) with the number of up-regulated (in orange), down-regulated (in blue), and total number of genes involved in the gene set (in black). (**F**) Venn diagram of overlapping significant GO terms in myofiber-specific RNA sequencing between patients with NEM6 and *Kbtbd13*(R408C) mice. Blue circles represent slow-twitch type I myofibers from patients with NEM6 and *Kbtbd13*(R408C) mice, and green circles represent fast-twitch type IIa myofibers. Overlapping GO terms between *Kbtbd13*(R408C) mice and patients with NEM6 for slow-twitch type I (top) and fast-twitch type IIa myofibers (bottom) are also shown.

To verify that the transcriptional changes translate to changes at the protein level, we performed bulk proteomics on 9-month-old *Kbtbd13*(R408C) male mice and compared those with bulk transcriptomics. Figure 6A displays the PCA plots for soleus bulk RNA sequencing and proteomic data. Analyses revealed 3377 DEGs and 339 differentially expressed proteins (DEPs), with 194 gene/proteins overlapping between both datasets (Fig. 6B). We next performed gene set enrichment analysis for the DEGs and DEPs using the Enrichr tool (Fig. 6C) (*45*–*47*). Six of these 10 most significant GO terms overlapped between the transcriptomic and proteomic datasets (highlighted in yellow), mainly relating to mitochondrial function and muscle contraction. Furthermore, the Venn diagram between the top and bottom panels of Fig. 6C highlights the overlap of 40 GO terms between the significant ($P < 0.05$) biological processes identified on the basis of the DEGs and DEPs. We concluded that 1-month-old mice represented a prephenotype stage, 3-month-old mice represented disease onset, and 9-month-old mice represented an overt-phenotype stage, which we then studied to develop a potential therapeutic for NEM6.

Kbtbd13 deficiency is well tolerated in mouse skeletal muscles

We hypothesized that reducing *Kbtbd13* transcript abundance might prevent the onset of disease or reverse the disease phenotype on the basis of our previous work on a *Kbtbd13* KO mouse model that displayed no major morphological or functional phenotypes by 9 months of age (*29*), suggesting that *Kbtbd13* deficiency is well tolerated. Thus, to confirm that *Kbtbd13* knockdown is tolerated throughout life, we performed a natural history study in homozygous *Kbtbd13* KO mice at 3, 9, and 18 months of age through analysis of morphological and functional parameters of soleus muscle, because this was the most affected muscle in the *Kbtbd13*(R408C) model. Myofiber-type distribution and CSA analysis showed no differences compared to WT mice (fig. S5, A and B), and no nemaline rods were observed at 3, 9, or 18 months (fig. S5C). Furthermore, *Kbtbd13* deficiency did not affect maximal muscle tension in 3-, 9-, or 18-month-old mice (fig. S5D), and soleus muscle relaxation kinetics were also unaffected at 3 and 9 months, with mildly affected relaxation kinetics at 18 months (fig. S5E). Together, these findings indicate that *Kbtbd13* deficiency was well tolerated in skeletal muscles, with no major morphological or functional consequences. We therefore pursued a therapeutic approach to knock down mutant *Kbtbd13* in *Kbtbd13*(R408C) mice.

Prophylactic *Kbtbd13* knockdown prevents phenotype onset in *Kbtbd13*(R408C) soleus muscle

We first tested whether knocking down *Kbtbd13* before disease onset prevents phenotype onset. We injected the soleus muscles of 1-month-old male mice with a single dose of AAV9 containing a short-hairpin RNA (shRNA) against *Kbtbd13* (AAV9-sh*Kbtbd13*) at a dose of 2.4×10^{11} viral particles (V.P.). (Fig. 7A). Quantitative polymerase chain reaction (qPCR) analysis showed that a single intramuscular injection with AAV9-sh*Kbtbd13* was sufficient to knock down *Kbtbd13* by 84 ± 3% 8 weeks after treatment (Fig. 7B, left panel). In Fig. 7B (right panel), we show a representative image of a treated soleus muscle expressing the green fluorescent protein reporter fused to the short hairpin construct. Note that the whole muscle was transfected. Eight weeks after injection, *Kbtbd13*(R408C) soleus muscle mass and CSA were comparable to those of WT mice (fig. S6A, bottom left and bottom right panels, respectively). *Kbtbd13* knockdown prevented the myofiber-type shift toward an oxidative phenotype (Fig. 7C) and prevented the formation of nemaline rods by 99.95 ± 0.02% (Fig. 7D). To investigate the pathways that were involved in the clearance of nemaline rods, we analyzed by qPCR the transcriptional changes in 22 key gene markers for the main protein quality control systems: the ubiquitin proteasome system (UPS) and the macroautophagy system. *Kbtbd13* knockdown up-regulated 17 of the 22 analyzed genes as compared with the WT and untreated groups (Fig. 7G). In addition, both *Cullin 3* (*Cul3*) and *Ring-box 1* (*Rbx1*), which are substrate adaptors for *Kbtbd13*, were down-regulated to a similar magnitude to *Kbtbd13*, suggesting that they were at least partially regulated by *Kbtbd13* expression. *Kbtbd13* knockdown also partially restored the sarcomeric gene expression profile at 3 months (fig. S6B). Eight weeks after treatment, fast-twitch type IIa myofiber CSA was comparable to WT, and slow-twitch type I myofiber CSA was reduced to levels below those of WT mice (Fig. 7E, with whole muscle myofiber-type distribution shown in Fig. 8F).

Last, although *Kbtbd13* knockdown at a prephenotype stage did not fully prevent the development of muscle weakness (Fig. 7H), it did prevent the development of impaired muscle relaxation kinetics (Fig. 8I). In summary, prophylactic *Kbtbd13* knockdown was sufficient to prevent nemaline rod accumulation, slow-twitch type I myofiber predominance and hypertrophy, and slow muscle relaxation kinetics, although it did not prevent the development of muscle weakness.

Kbtbd13 knockdown after phenotype onset restores muscle morphology and function

Because patients with NEM6 are typically diagnosed when they are symptomatic, we tested the ability of *Kbtbd13* knockdown to revert an established NEM6 phenotype. AAV9-sh*Kbtbd13* (4.74×10^{11} V.P.) was injected into the soleus muscles of *Kbtbd13*(R408C) male mice at either 3 or 7 months of age, and short-term (8 weeks in the 7-month-old mice) and long-term (24 weeks in the 3-month-old mice) effects were monitored (Fig. 8A). A single intramuscular injection down-regulated *Kbtbd13* in treated soleus muscles by 88 ± 2 and 86 ± 2% in the short-term and long-term studies, respectively (Fig. 8B, left panel). Homogeneous expression of sh*Kbtbd13* was seen in both short term– and long term–treated mice (Fig. 8B, right panel).

Short-term treatment did not affect the whole muscle weight or CSA, whereas long-term treatment normalized both (fig. S6C, bottom left and right panels). Although short-term treatment did not restore normal myofiber-type distribution, long-term treatment did (Fig. 8C, middle and right panels). Short- and long-term *Kbtbd13* knockdown resulted in the clearance of nemaline rods by 92.7 ± 2.2 and 99.8 ± 0.05%, respectively (Fig. 8D). Like prephenotype treatment, long-term knockdown up-regulated macroautophagy and UPS markers (Fig. 8G) as compared with WT and untreated *Kbtbd13*(R408C) mice. Long-term knockdown also partially restored sarcomeric gene expression by up-regulating *skeletal muscle actin alpha 1* (*Acta1*), *troponin T3* (*Tnnt3*), *nebulin* (*Neb*), *Klech-like family member 40* (*Klhl40*), and *neural precursor cell expressed, developmentally down-regulated 8* (*Nedd8*) and down-regulating *tropomyosin 1* (*Tpm1*) and *Tpm2* (fig. S6D). In addition, *Kbtbd13* substrate adaptors *Cul3* and *Rbx1* were down-regulated in both short term– and long term–treated mice. However, Cul3 and Rbx1 protein abundances were comparable to WT and *Kbtbd13*(R408) after treatment (fig. S6E). Although short-term *Kbtbd13* knockdown did not restore myofiber CSA, long-term treatment normalized slow-twitch type I and

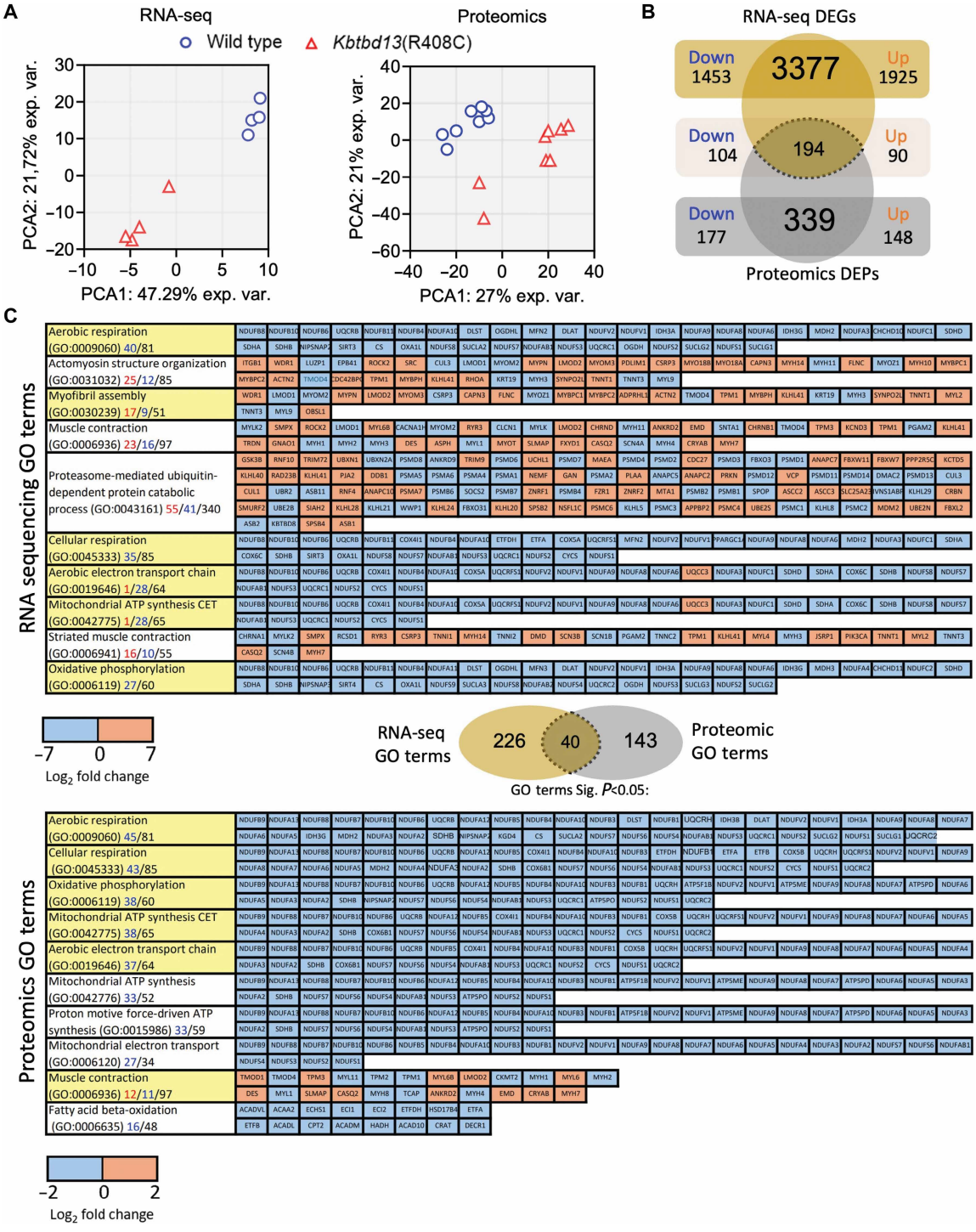

Fig. 6. *Kbtbd13*(R408C) mouse soleus muscle transcriptomics and proteomics. (**A**) PCA plots showing the distribution of WT and *Kbtbd13*(R408C) soleus RNA sequencing (RNA-seq; left) and proteomic samples (right) based on the first two principal components (for RNA sequencing, $n = 4$ soleus muscles per group; for proteomics, $n = 8$ soleus muscles per group). (**B**) Venn diagram highlighting soleus RNA sequencing DEGs (top), soleus proteomic DEPs (bottom), and overlapping genes and proteins differentially expressed in both datasets (middle). The number of overlapping DEGs and proteins that are up-regulated (right, orange) or down-regulated (left, blue) is indicated. (**C**) The top and bottom panels represent a list of the top 10 enriched biological processes based on the significant DEGs and proteins for the soleus muscles of *Kbtbd13*(R408C) mice as compared with soleus WT muscles. Highlighted in yellow are the overlapping GO terms between RNA sequencing and proteomic data. Cells on the right of every significant biological process represent a gene or protein involved in the shown biological processes. In light blue, the genes/proteins that are down-regulated and, in orange, the genes/proteins that are up-regulated. Note that next to each GO term, the numbers of up-regulated (in red) and down-regulated (in blue) and the total number of genes involved in the gene set (in black) are displayed. The middle panel between the RNA sequencing and proteomic datasets shows a Venn diagram of the significant biological processes for the RNA sequencing and proteomic dataset with the shared common processes between both datasets.

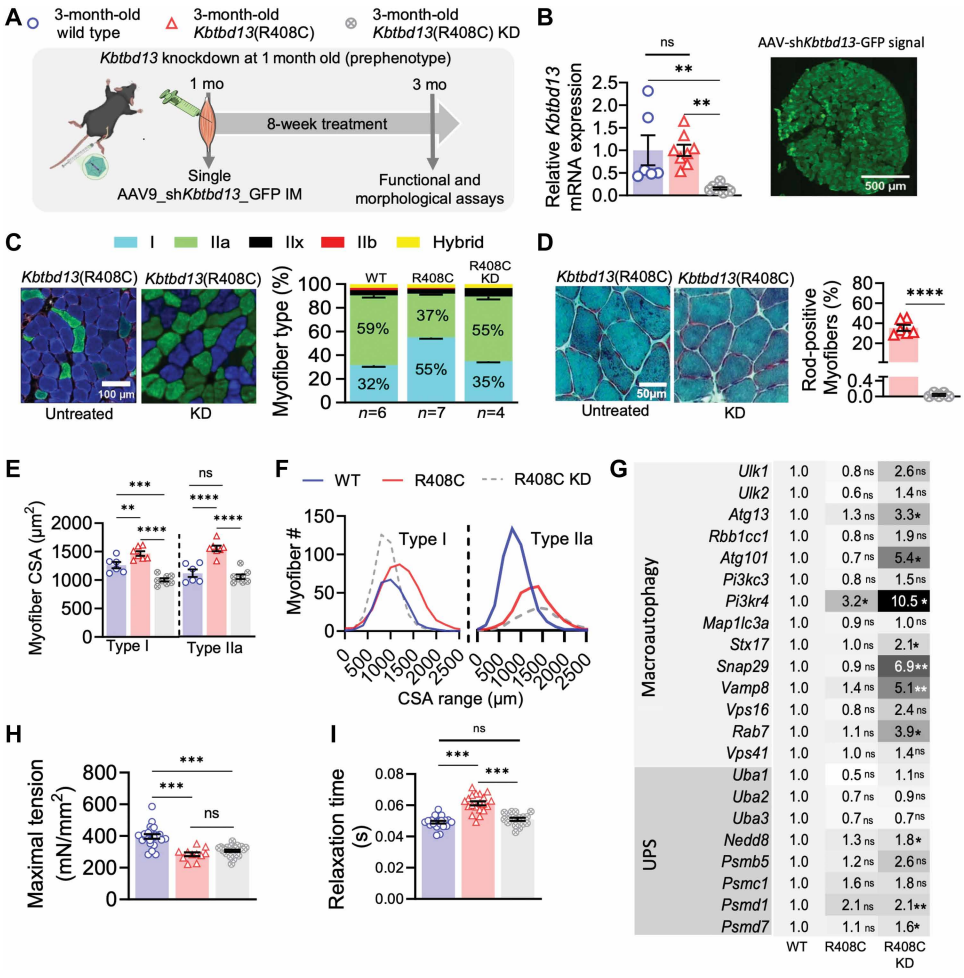

Fig. 7. Therapeutic effect of prophylactic *Kbtbd13* knockdown in 1-month-old *Kbtbd13*(R408C) mice, evaluated 2 months after treatment. (**A**) Schematic representation of the intramuscular injection pipeline used for *Kbtbd13* short hairpin–mediated *Kbtbd13* knockdown (KD) (AAV_sh*Kbtbd13*_GFP). Mice were injected at 1 month of age with a dose of $2.4*10^{11}$ V.P. and morphologically and mechanically characterized at 3 months of age. Created in part with BioRender.com. (**B**) *Kbtbd13* transcript expression in *Kbtbd13*(R408C) soleus muscles after single intramuscular injection with AAV9_sh*Kbtbd13*_GFP (left) and representative image of the treated soleus muscle expressing the GFP reporter (right). Scale bar, 500 µm. (**C**) Left panel: Representative images of untreated and short-term KD in *kbtbd13*(R408C) soleus muscle, stained with MHC antibodies for fiber-type percentage quantification. Scale bar, 100 µm. Right panel: Whole soleus muscle myofiber-type distribution calculated from soleus muscles stained for MHCs [$n = 6$ for WT, $n = 7$ for *Kbtbd13*(R408C), and $n = 4$ for *Kbtbd13*(R408C) KD]. (**D**) Left panel: Representative images of soleus muscles stained with modified Gömöri trichrome for nemaline rod visualization. Right panel: Calculation of nemaline rod–positive myofibers in the whole soleus muscle as a percentage of total muscle myofibers. $n = 6$ for *Kbtbd13*-(R408C), and $n = 4$ for *Kbtbd13*(R408C) KD. (**E**) Soleus slow-twitch type I and fast-twitch type IIa single myofiber CSA, respectively, as measured by whole muscle immunolabeling. (**F**) Calculation of slow-twitch type I and fast-twitch type IIa soleus single myofiber CSA distribution. For (E) and (F), $n = 6$ for WT, $n = 7$ for *Kbtbd13*(R408C), and $n = 8$ for *Kbtbd13*(R408C) KD. (**G**) Heatmap for qPCR gene expression profile (fold change) for genes involved in macroautophagy and UPS. Comparisons: R408C versus WT and R408C KD versus WT. $*P \leq 0.05$; $**P \leq 0.01$. (**H**) In vitro soleus maximal tensions measured at 150-Hz stimulation. $n = 22$ for WT, $n = 11$ for *Kbtbd13*(R408C) untreated, and $n = 24$ for *Kbtbd13*(R408C) KD. (**I**) In vitro soleus relaxation times after 150-Hz stimulation. $n = 21$ for WT, $n = 20$ for *Kbtbd13*(R408C) untreated, and $n = 16$ for *Kbtbd13*(R408C) KD. Statistical analysis: A one-way ANOVA with Tukey's multiple comparison test was performed on data for (B), (C), (E), (H), and (I). A paired *t* test was performed for data in (D). A two-way ANOVA with Dunnett's multiple comparison test was performed for data in (G). Significance was set to $P < 0.05$ ($*P < 0.05$, $**P < 0.01$, $***P < 0.001$, and $****P < 0.0001$), and all data are presented as the means ± SEM.

fast-twitch type IIa myofiber CSA (Fig. 8E). In Fig. 8F, we show the whole muscle myofiber-type distribution for slow-twitch type I and fast-twitch type IIa myofibers, respectively.

Last, we investigated the effect of *Kbtbd13* knockdown on muscle contractility. Long-term *Kbtbd13* knockdown restored maximal muscle tension (Fig. 8H), and both short- and long-term treatment restored muscle relaxation kinetics (Fig. 8I). Together, these results indicate that *Kbtbd13* knockdown after phenotype onset was sufficient to revert nemaline rod accumulation and slow-twitch type I myofiber predominance and hypertrophy, and at a functional level, *Kbtbd13* knockdown was sufficient to restore muscle contractility and muscle relaxation kinetics in *Kbtbd13*(R408C) mice.

DISCUSSION

Here, we showed that the *Kbtbd13*(R408C) mouse model recapitulates the phenotype of patients with NEM6 at the morphological, nanostructural, and functional levels. Figure S7 summarizes our study design and highlights the main outcome measures. At the transcriptional level, our data indicate that both mouse and human muscles exhibit a myofiber type–specific transcriptional phenotype. Although mice and humans have a low transcriptional profile similarity at a myofiber type–specific level, when comparing different myofiber types, we observed a higher similarity, especially between human type IIa and mouse type I myofibers. Last, we showed that prophylactic and therapeutic knockdown of *Kbtbd13* prevents NEM6 histopathological hallmarks and impaired muscle relaxation kinetics, which lead to the main complaint of patients. Thus, our data highlight the promise of *Kbtbd13* knockdown as a therapeutic strategy for patients with NEM6, for whom there is currently no targeted therapy.

Myofiber-type changes and aberrant protein aggregation (nemaline rods) are two main histopathological changes characteristic of NEM6 muscle that have profound effects on skeletal muscle function. If the root cause of these changes is well understood, therapeutic interventions to prevent or reverse them can be developed. Data from the *Kbtbd13*(R408C) mouse model showed that myofiber-type

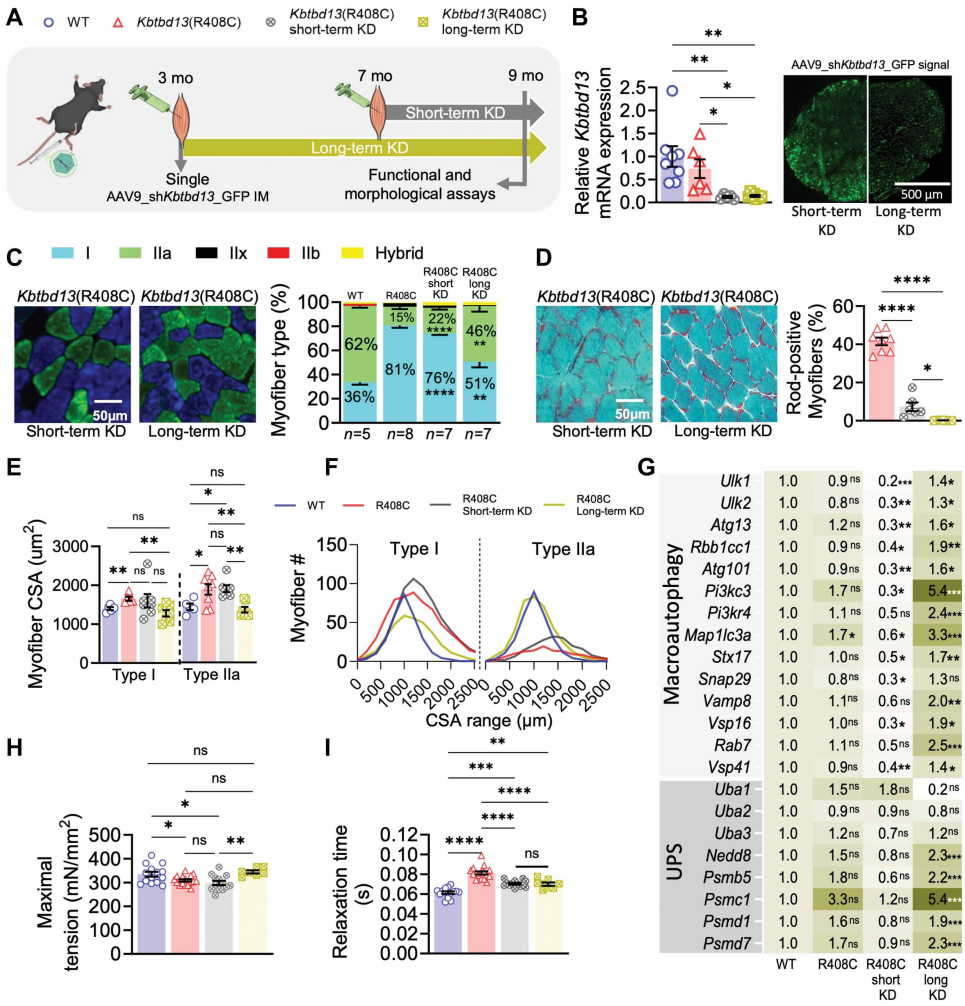

Fig. 8. Therapeutic short- and long-term *Kbtbd13* knockdown in 3- and 7-month-old *Kbtbd13*-(R408C) mice, evaluated in 9-month-old muscles. (**A**) Schematic representation of the intramuscular (IM) injection pipeline used for *Kbtbd13* short- and long-term short hairpin–mediated *Kbtbd13* knockdown (AAV_sh*Kbtbd13*_GFP). Mice were injected with a dose of 4.74×10^{11} V.P., at either 3 months of age (long-term knockdown) or 7 months of age (short-term knockdown), and morphologically and mechanically characterized at 9 months of age to study the effects of short- and long-term effects of *Kbtbtd13*(R408) knockdown. Created in part with BioRender.com. (**B**) Left panel: *Kbtbd13* transcript knockdown in *Kbtbd13*(R408C) soleus muscles after a single intramuscular injection with AAV9_sh*Kbtbd13*. Right panel: Representative images for short term– and long term–treated soleus muscle expressing the GFP reporter. Scale bar, 100 µm. (**C**) Left panel: Representative images of short-term knockdown and long-term knockdown in *kbtbd13*(R408C) soleus muscles, stained with MHC antibodies for fiber-type percentage quantification. Scale bar, 50 µm. Right panel: Whole soleus muscle myofiber type distribution calculated from soleus muscles stained for MHCs [n = 5 for WT, n = 8 for *Kbtbd13*(R408C), n = 7 for *Kbtbd13*(R408C) short-term knockdown, and n = 7 for *Kbtbd13*(R408C) long-term knockdown]. (**D**) Left panel: Representative images of soleus muscles stained with modified Gömöri trichrome for nemaline rod visualization. Right panel: Calculation of nemaline rod–positive myofibers in the whole soleus muscle as a percentage of total muscle myofibers. n = 8 for *Kbtbd13*(R408C), n = 6 for *Kbtbd13*(R408C) short-term knockdown, and n = 7 for *Kbtbd13*(R408C) long-term knockdown. (**E**) Soleus slow-twitch type I (left) and fast-twitch type IIa (right) single myofiber CSA, respectively, as measured by whole muscle immunolabeling. (**F**) Calculation of slow-twitch type I (left) and fast-twitch type IIa (right) soleus single myofiber CSA distribution. For (E) and (F), n = 5 for WT, n = 8 for *Kbtbd13*(R408C), n = 7 for *Kbtbd13*(R408C) short-term knockdown, and n = 7 for *Kbtbd13*(R408C) long-term knockdown. (**G**) Heatmap of qPCR gene expression profile (fold change) for genes involved in macroautophagy and UPS. Comparisons: R408C versus WT, R408C short KD versus WT, and R408C long KD versus WT: *$P \leq 0.05$, **$P \leq 0.01$, and ***$P \leq 0.001$. (**H**) In vitro soleus maximal tensions measured at 150-Hz stimulation. n = 14 for WT, n = 16 for *Kbtbd13*(R408C) untreated, n = 13 for *Kbtbd13*(R408C) short-term knockdown, and n = 8 for *Kbtbd13*(R408C) long-term knockdown. (**I**) In vitro soleus relaxation times after 150-Hz stimulation. n = 15 for WT, n = 16 for *Kbtbd13*(R408C) untreated, n = 13 for *Kbtbd13*(R408C) short-term knockdown, and n = 8 for *Kbtbd13*(R408C) long-term knockdown. Statistical analysis: A one-way ANOVA with Tukey's multiple comparison test was performed on data for (B), (C), (E), (H), and (I). A two-way ANOVA with Dunnett's multiple comparison test was performed for data in (G). A paired t test was performed for data in (D). Significance was set to $P < 0.05$ (*$P < 0.05$, **$P < 0.01$, ***$P < 0.001$, and ****$P < 0.0001$), and all data are presented as the means ± SEM.

composition was normal at 1 month, shifted toward an oxidative phenotype in young adulthood (3-month-old mice), and then plateaued in adulthood (9 months), which correlated with nemaline rod aggregation. Typically, muscle morphological and functional changes due to pathological gene variants are rarely reversible. Few studies have shown partial improvement in muscle morphology and function in NM models after testing various therapeutic strategies (*48*–*55*). Because we found that *Kbtbd13* was dispensable for muscle function, we developed a relevant therapeutic effect by knocking down *Kbtbd13* transcript in *Kbtbd13*(R408C) mice, which led to restoration of muscle morphology and improvement in contractile function. One factor that could explain the restoration of muscle force is the clearance of nemaline rods. Such protein aggregates occupy the physical space in the sarcomere; thus, fewer contractile structures are available for force development. Although clinical disease severity in NM has been shown to poorly correlate with the number of nemaline rods in different NMs (*56*), a preclinical study in an NM mouse model caused by a *Tpm3* variant showed a strong correlation between the number of nemaline rods and muscle weakness (*57*). However, unlike restoration of muscle tension, the clearance of nemaline rods cannot explain the restoration of normal muscle relaxation kinetics, because many other NMs and congenital myopathies present with rod formation but not with muscle relaxation problems.

Furthermore, in the *Kbtbd13*(R408C) mouse model, the normalization of myofiber-type distribution after treatment also does not explain the restoration of muscle relaxation kinetics: Both short- and long-term knockdown had the same effect on relaxation kinetics of the soleus muscle; however, only in the long term–treated group did we observe a restoration of myofiber-type distribution.

Additionally, in biopsies of patients with NEM6, we have previously shown comparable impairment in relaxation kinetics in both slow- and fast-twitch myofibers (*29*). Therefore, myofiber-type changes alone cannot account for the restoration of normal muscle relaxation in *Kbtbd13*(R408C) mice. A more likely explanation for the normalization of muscle relaxation kinetics is the normalization of thin-filament stiffness. As shown in our previous work (*29*), *Kbtbd13*(R408C) stiffens the thin filament, leading to impaired muscle relaxation kinetics. We propose that *Kbtbd13* knockdown normalizes thin-filament stiffness by lowering the amount of mutant protein, thus contributing to the normalization of muscle relaxation kinetics.

Although we observed this effect in slow-twitch soleus muscles, we did not observe the same phenotype in the fast-twitch EDL muscles of *Kbtbd13*(R408C) mice. The difference in phenotypes is likely due to differences in the proportions of myofiber types between the soleus and EDL muscles. On the basis of the results of our bulk and myofiber type–specific RNA sequencing data, we propose that mainly slow-twitch type I and fast-twitch type IIa myofibers are affected and that fast-twitch IIx and type IIb myofibers are relatively spared in *Kbtbd13*(R408C) mice.

Mouse EDL muscle is composed mainly of fast-twitch type IIb and IIx myofibers, whereas humans do not express MYH4, the gene encoding fast-twitch type IIb myosin (*58*). Single-myofiber transcriptome analysis showed strong similarities between mouse and human slow-twitch type I and fast-twitch type IIa myofibers, consistent with previous studies of contractile and metabolic properties (*59*, *60*). For example, genes involved in mitochondrial and metabolic processes are highly expressed in mouse fast-twitch type IIa and human slow-twitch type I myofibers. On the basis of these similarities, we compared transcriptomic profiles across myofiber types, identifying shared expression patterns between human type IIa and mouse type I myofibers, as well as between human type I/IIa myofibers and the mouse soleus muscle transcriptome. We therefore further analyzed the possible transcriptional similarities and differences by comparing our data across different myofiber types, which revealed that human fast-twitch type IIa myofibers are most similar to mouse slow-twitch type I myofibers and that both slow-twitch type I and fast-twitch type IIa human myofibers share transcriptional similarity to the mouse whole soleus muscle transcriptome. This is because the soleus muscle exclusively expresses slow-twitch type I and fast-twitch type IIa myofibers, with little to no fast-twitch type IIx and fast-twitch type IIb fibers that are not expressed in humans. This is supported by previous work characterizing the transcriptional profile across different mouse backgrounds and human quadriceps biopsies (*44*). Therefore, we feel that our mouse model, and especially the soleus muscle, provides a reliable transcriptional profile, on which we could further study the implications of the *Kbtbd13*:p.Arg408Cys variant, and it underscores the value of cross-species RNA sequencing in identifying potential therapeutic targets for muscle-related diseases.

Like human patients with NEM6 who show onset of symptoms during adolescence, in this study, the myopathic changes observed in *Kbtbd13*(R408C) mice were seen from 3 months onward. Although *Kbtbd13* is expressed from birth, its expression is not needed for embryonic or postnatal development in mice (*29*). A possible explanation as to why we observed the development of evident phenotype at 3 months was the time-dependent *Kbtbd13* expression profile, where we observed an about ninefold increase in *Kbtbd13* expression at 1 month as compared with postnatal (7 days old) and adult (3 to 18 months old) mice (fig. S1F). Mutant mice had a fourfold lower *Kbtbd13* expression than WT mice at 1 month of age, resulting in down-regulation of most sarcomeric genes encoding thin-filament proteins typically involved in NEM. Although mRNA expression of KBTBD13 substrate adaptors *CUL3* and *RBX1* was down-regulated, CUL3 and RBX1 protein analyses showed comparable expression between WT and untreated *Kbtbd13*(R408C) mice, suggesting that the clearance of rods after *Kbtbd13* knockdown was independent of CUL3 and RBX1 expression.

Sambuughin *et al.* (*30*) suggested that KBTBD13 might play a key role in regulating sarcomeric protein homeostasis, and the *Kbtbd13*:p.Arg408Cys variant has been predicted to disrupt the KBTBD13 β-propeller blade (*19*). This hypothesis is supported by our in vivo localization data, which suggest that the p.Arg408Cys variant loses its thin-filament localization and aggregates at the Z-disk and other regions in the sarcomere. Previous work on proteasomal dynamics in the sarcomere showed that the 20*S* proteasome subunit localizes to the Z-disk, where it regulates protein turnover and sarcomeric genesis (*61*), raising the possibility, although speculative, that mutant KBTBD13 aggregation in the Z-disk may impair the normal function of protein quality control systems and consequently induce nemaline rod formation. Impairment in these systems has been shown to induce muscle dysfunction and protein aggregation (*62*). This could be supported by the strong effect of *Kbtbd13* knockdown on nemaline rod clearance and regulation of key markers for the UPS and macroautophagy system. Although most analyzed markers had normal expression pretreatment, nemaline rod accumulation was evident in all assessed muscles, supporting the notion that deregulation rather than the lower activity of this pathway could be the culprit. It is known that deregulation of the UPS contributes to pathological changes in congenital myopathies (*63*, *64*). As with impaired UPS, impaired autophagy flux has been shown in various congenital myopathies to contribute to muscle dysfunction (*65*–*68*), and a decline in autophagy can lead to reduced clearance of damaged proteins (*69*), further supporting the notion that the mutant transcript or protein is likely to be toxic to skeletal muscle.

Here, we showed a strong therapeutic effect by down-regulating the expression of a transcript encoding a gain-of-function variant in a clinically relevant mouse model for NEM6. Although NEM6 is a rare disorder and very few patients have been diagnosed worldwide, our therapeutic approach may apply to other neuromuscular disorders caused by gain-of-function variants. Furthermore, over the past 10 years, groundbreaking advances in gene therapy have enabled effective treatment of previously untreatable genetic neuromuscular disorders. AAV-mediated therapies are rapidly evolving, and promising results have been obtained in spinal muscular atrophy, myotonic dystrophy, and Duchenne muscle dystrophy (*70*). Although severe clinical adverse effects related to viral load and toxicity have raised concerns (*39*), these are areas of active research as clinicians, researchers, and industry seek to address these concerns by identifying the risks of AAV in patient populations, by screening preexisting conditions, and by designing optimal approaches to manage adverse effects (*71*). Furthermore, advances in AAV capsid development have shown promising results by lowering viral doses by 10-fold yet achieving a comparable therapeutic effect as with traditional AAVs (*72*–*74*). In humans, *KBTBD13* is exclusively expressed, and at very low levels, in striated muscle tissue [KBTBD13 protein expression summary—The Human Protein Atlas (*28*)]. Therefore, a relatively low dose of AAV delivered systemically might theoretically have a positive effect on the phenotype of patients with NEM6.

A limitation of our study is that we designed a full knockdown of *Kbtbd13* as a therapeutic approach. Although complete knockdown of *Kbtbd13* was well tolerated and homozygous *Kbtbd13*(R408C) mice benefited from this approach, patients with NEM6 carry single gain-of-function variants, and we cannot infer from our data what the effect would be of knocking down both WT and mutant alleles in humans. Future studies are needed to assess the effect of allele-specific knockdown as a therapeutic strategy to maintain the expression of the WT allele. Another limitation of our study is that the long-term knockdown treatment lasted 6 months. Future studies should address how long, beyond 6 months, a single knockdown treatment remains effective, because current AAV-based approaches can only be given as one-time doses. In addition, we tested the efficacy of local, intramuscular injections rather than that of systemic delivery.

Despite these limitations, the robust therapeutic benefit observed with the knockdown of *Kbtbd13* across molecular, histological, and functional outcomes supports the continued development of *KBTBD13*-targeted strategies. These findings provide a strong foundation for future optimization toward clinically translatable therapies for NEM6, systemic intravenous delivery to target multiple muscles. We aim to test this in future studies in patients with NEM6 once we have developed a successful allele-specific approach.

MATERIALS AND METHODS

Study design

This study aimed to perform a natural history characterization of NEM6 in a clinically relevant mouse model at 1, 3, 9, and 18 months to establish the age of disease onset, rate of progression, and therapeutic windows and then to test the efficacy of *Kbtbd13* knockdown as a potential therapeutic approach. We applied a multimodal approach by using whole mouse muscle in vitro mechanical measurements, histological characterization, in vitro and in vivo protein localization studies, small-angle x-ray diffraction studies, and bulk and muscle fiber–specific transcriptomics to characterize disease onset, progression, and pathogenesis. As a therapeutic strategy, we performed *Kbtbd13* knockdown by intramuscular injections with AAV9-shRNA. The primary outcomes included restoration of muscle morphology, including nemaline rod content and myofiber-type distribution, and muscle contractile function, including maximal force, maximal tension, and muscle relaxation kinetics. The group sizes for muscle mechanical measurements were estimated by a power analysis, performed using the magnitude of weakness in leg muscles that we found earlier in in vitro force measurements of WT and *Kbtbd13*(R408C) mice (*29*): 15% in soleus (~10% in EDL). With a standard deviation of about 12% in the WT group and about 12% in the *Kbtbd13*(R408C) group, a significance of $\alpha = 0.05$, and a power of $n = 0.8$, we calculated that we needed 11 animals per group. We considered a tissue loss of 20%; therefore, we calculated that we needed 14 mice per group for the muscle mechanical measurements. Results were compared to those from studies on human NEM6 muscle biopsies to ensure that the mouse model recapitulated the main human NEM6 morphological characteristics. Muscles that showed >10% run down in force during the force-frequency protocol were excluded from analysis in the mechanical measurement experiments. *Kbtbd13* knockdown was accomplished by intramuscular injections with AAV9-shRNA, with primary outcomes including restoration of muscle morphology and muscle function.

Study approval

Experimental procedures for human studies were approved by the institutional ethics committee and performed in accordance with ethical standards laid down in the Declaration of Helsinki. All biopsies were collected following informed consent from the patients or their guardians and were approved by the Radboud University Institutional Review Board. All animal experiments were performed in accordance with the national guidelines approved by the Central Committee for Animal Experiments (AVD1140020209865) and the Institute of Animal Welfare (IvD) of the Vrije Universiteit Amsterdam. *Kbtbd13*(R408C) and *Kbtbd13* KO mouse models were generated as previously described (*29*).

Human muscle biopsy characterization

For histological analysis, 8-μm muscle sections were collected using a Leica CM3050S cryostat. Muscle biopsy specimens were processed in regular diagnostics for routine histological reactions and stained for modified Gömöri trichrome for nemaline rod visualization and ATPase at pH 10.3, 4.6, and 4.3 for fiber-type distribution. Morphometrics were performed to establish the myofiber CSA and percentages of each fiber type.

Intramuscular injections for *Kbtbd13* knockdown

For the *Kbtbd13* knockdown studies, we developed an AAV9 containing a short hairpin against the *Kbtbd13* transcript (AAV9-sh*Kbtbd13*) and injected *Kbtbd13*(R408C) mice intramuscularly in the soleus muscle. Briefly, 1-month-old (predisease onset) and 3- and 7-month-old (overt phenotype; short and long-term treatment, respectively) male homozygous *Kbtbd13*(R408C) mice were chosen for this experiment. Mice were deeply anesthetized by isoflurane administration (5% isoflurane + 0.2 liter/min O_2 and 0.2 liter/min air) and placed in a prone position over a temperature-regulated heat pad and kept under anesthesia by isoflurane administration (3% isoflurane + 0.2 liter/min O_2 and 0.2 liter/min air) for the remainder of the procedure. The right calf was shaved using an electrical trimmer to visualize the soleus/gastrocnemius muscle and Achilles tendon complex, and the area was thoroughly disinfected with 70% alcohol. For the virus injection, we designed a modified Hamilton syringe (25 μl, model 702N SYR, Cemented NDL, 22s ga, 2 in, point style 5) attached to a 15-cm silicon tube (HELI60-795-03) on one end, and on the injection side, we attached a 34-gauge needle (Nanopass, Terumo). One-, 3-, and 7-month-old mice were injected with 5 to 10 μl of AAV9-sh*Kbtbd13* at final concentrations of 2.4×10^{11} V.P. (1-month-old mice) and 4.73×10^{11} V.P. (3- and 7-month-old mice) and incubated for a period of 8 weeks (short-term treatment) and 24 weeks (long-term treatment). The injection procedure was as follows: The soleus muscle belly was localized on the lateral side along the Achilles tendon. One researcher inserted the modified 34-gauge needle into the soleus muscle following the mediolateral side of the Achilles tendon at a 30° angle. Once the needle was inserted properly (~2 mm), a second researcher pressed the plunger at a rate of 0.5 μl/s to ensure a homogeneous distribution of the virus. After injecting the required AAV amount, we waited for 5 s before slowly retracting the syringe to avoid leakage. After injection, mice were immediately transferred to their respective cages to wake up from the anesthesia. After the indicated time periods, 3- and 9-month-old groups were euthanized, and soleus muscles were immediately dissected and transferred to an in vitro test apparatus for contractile measurements (Aurora Scientific), whereas the gastrocnemius muscle was cryopreserved for molecular assays.

Mouse in vivo functional assays

Mice were run on an indirect calorimetry treadmill (TSE Systems) at 3 to 4 and 8 to 9 months. Mice underwent a treadmill running protocol. Before each treadmill test, mice were acclimated to the treadmill for 1 day before the test. Acclimation consisted of the following: 0 m/min, 5 min; 6 m/min, 5 min; 9 m/min, 2 min; 12 m/min, 2 min. The running protocol consisted of the following: 0 m/min, 5 min; 10 m/min, 5 min; 11 m/min, 5 min; 12 m/min, 5 min; 13 m/min, 5 min; 14 m/min, 5 min; 15 m/min, 5 min; 20 m/min, 20 min or until exhaustion was reached. Exhaustion was defined as the point at which mice maintained continuous contact with the shock grid for 5 s or when there were 20 visits to the shock grid within a 60-s period. During testing, gas was collected continuously and analyzed every 5 s. PhenoMaster software (TSE Systems) recorded and calculated oxygen consumption (VO_2), carbon dioxide consumption (VCO_2), the respiratory exchange ratio (RER), distance run, and visits to the shock grid. The VO_{2max} was determined by the peak VO_2 reached. Maximum running speed was defined as the treadmill speed at which VO_{2max} was achieved.

Mouse muscle tissue collection

Mice were deeply anesthetized by isoflurane (5% isoflurane + 0.2 liter/min O_2 and 0.2 liter/min air) administration. Cervical dislocation was performed after the absence of a foot reflex was confirmed. Soleus, EDL, diaphragm, quadriceps, gastrocnemius, and tibialis anterior muscles were carefully dissected and cryopreserved in supercooled isopentane (1.06056, Uvasol) and kept at −80°C.

Statistical analysis

Biological replicates were collected for all experiments, unless otherwise noted. Statistical analyses were performed using GraphPad Prism (GraphPad Software, version 8.1, San Diego, CA). For natural history characterization studies, comparisons between WT and *Kbtbd13*(R408C) animals were performed either at individual ages or across multiple ages/time points depending on the experimental design. Two-group comparisons at a single age were analyzed using unpaired Student's *t* tests when assumptions of normality and equal variance were met. For analyses involving genotype comparisons across multiple ages and time points and or multiple variables, a one-way or two-way analysis of variance (ANOVA) with appropriate multiple-comparison post hoc testing was performed as applicable to the study design. For experiments involving three or more groups, including WT versus *Kbtbd13*(R408C) versus *Kbtbd13*(R408C) prephenotype treatment groups or WT versus *Kbtbd13*(R408C) versus short-term treatment versus long-term treatment groups, a one-way or two-way ANOVA followed by multiple-comparison correction was used as appropriate. The normality of data distribution was assessed using the Shapiro-Wilk or comparable normality tests. When datasets failed normality testing, nonparametric alternatives were applied, including Mann-Whitney tests for two-group comparisons and Kruskal-Wallis tests with appropriate post hoc analyses for experiments involving three or more groups. Data are presented as the means ± SEM, unless otherwise indicated. Exact statistical tests, sample sizes (*n*), multiple-comparison methods, and significance thresholds used for each experiment are detailed in the corresponding figure legends. Specific statistical methods and details are listed in each figure legend.

Supplementary Materials

The PDF file includes:
Figs. S1 to S7
Tables S1 to S4
Legend for data file S1
References (*76*–*92*)

Other Supplementary Material for this manuscript includes the following:
Data file S1
MDAR Reproducibility Checklist

REFERENCES AND NOTES

1. K. Huang, F. F. Bi, H. Yang, Corrigendum: A systematic review and meta-analysis of the prevalence of congenital myopathy. *Front. Neurol.* **13**, 857959 (2022).
2. I. Colombo, M. Scoto, A. Y. Manzur, S. A. Robb, L. Maggi, V. Gowda, T. Cullup, M. Yau, R. Phadke, C. Sewry, H. Jungbluth, F. Muntoni, Congenital myopathies: Natural history of a large pediatric cohort. *Neurology* **84**, 28–35 (2015).
3. C. Wallgren-Pettersson, C. A. Sewry, K. J. Nowak, N. G. Laing, Nemaline myopathies. *Semin. Pediatr. Neurol.* **18**, 230–238 (2011).
4. A. K. Brownell, J. J. Gilbert, D. T. Shaw, B. Garcia, G. F. Wenkebach, A. K. Lam, Adult onset nemaline myopathy. *Neurology* **28**, 1306–1309 (1978).
5. N. Fukuhara, T. Yuasa, T. Tsubaki, S. Kushiro, N. Takasawa, Nemaline myopathy: Histological, histochemical and ultrastructural studies. *Acta Neuropathol.* **42**, 33–41 (1978).
6. E. Shahar, R. C. Tervo, E. G. Murphy, Heterogeneity of nemaline myopathy. A follow-up study of 13 cases. *Pediatr. Neurosci.* **14**, 236–240 (2004).
7. M. M. Ryan, C. Schnell, C. D. Strickland, L. K. Shield, G. Morgan, S. T. Iannaccone, N. G. Laing, A. H. Beggs, K. N. North, Nemaline myopathy: A clinical study of 143 cases. *Ann. Neurol.* **50**, 312–320 (2001).
8. D. Sanoudou, A. H. Beggs, Clinical and genetic heterogeneity in nemaline myopathy—A disease of skeletal muscle thin filaments. *Trends Mol. Med.* **7**, 362–368 (2001).
9. X. Yin, C. Pu, Z. Wang, K. Li, H. Wang, Clinico-pathological features and mutational spectrum of 16 nemaline myopathy patients from a Chinese neuromuscular center. *Acta Neurol. Belg.* **122**, 631–639 (2022).
10. C. Gillies, J. Raye, U. Vasan, W. E. Hart, P. J. Goldblatt, Nemaline (rod) myopathy: A possible cause of rapidly fatal infantile hypotonia. *Arch. Pathol. Lab. Med.* **103**, 1–5 (1979).
11. K. Kondo, T. Yuasa, Genetics of congenital nemaline myopathy. *Muscle Nerve* **3**, 308–315 (1980).
12. R. D. McComb, W. R. Markesbery, W. N. O'Connor, Fatal neonatal nemaline myopathy with multiple congenital anomalies. *J. Pediatr.* **94**, 47–51 (1979).
13. S. A. Shafiq, V. Dubowitz, C. Peterson Hde, A. T. Milhorat, Nemaline myopathy: Report of a fatal case, with histochemical and electron microscopic studies. *Brain* **90**, 817–828 (1967).
14. C. Jirka, J. H. Pak, C. A. Grosgogeat, M. M. Marchetii, V. A. Gupta, Dysregulation of NRAP degradation by KLHL41 contributes to pathophysiology in nemaline myopathy. *Hum. Mol. Genet.* **28**, 2549–2560 (2019).
15. S. A. Sandaradura, A. Bournazos, A. Mallawaarachchi, B. B. Cummings, L. B. Waddell, K. J. Jones, C. Troedson, A. Sudarsanam, B. M. Nash, G. B. Peters, E. M. Algar, D. G. MacArthur, K. N. North, S. Brammah, A. Charlton, N. G. Laing, M. J. Wilson, M. R. Davis, S. T. Cooper, Nemaline myopathy and distal arthrogryposis associated with an autosomal recessive TNNT3 splice variant. *Hum. Mutat.* **39**, 383–388 (2018).
16. M. Yuen, S. A. Sandaradura, J. J. Dowling, A. S. Kostyukova, N. Moroz, K. G. Quinlan, V. L. Lehtokari, G. Ravenscroft, E. J. Todd, O. Ceyhan-Birsoy, D. S. Gokhin, J. Maluenda, M. Lek, F. Nolent, C. T. Pappas, S. M. Novak, A. D'Amico, E. Malfatti, B. P. Thomas, S. B. Gabriel, N. Gupta, M. J. Daly, B. Ilkovski, P. J. Houweling, A. E. Davidson, L. C. Swanson, C. A. Brownstein, V. A. Gupta, L. Medne, P. Shannon, N. Martin, D. P. Bick, A. Flisberg, E. Holmberg, P. Van den Bergh, P. Lapunzina, L. B. Waddell, D. D. Sloboda, E. Bertini, D. Chitayat, W. R. Telfer, A. Laquerriere, C. C. Gregorio, C. A. Ottenheijm, C. G. Bonnemann, K. Pelin, A. H. Beggs, Y. K. Hayashi, N. B. Romero, N. G. Laing, I. Nishino, C. Wallgren-Pettersson, J. Melki, V. M. Fowler, D. G. MacArthur, K. N. North, N. F. Clarke, Leiomodin-3 dysfunction results in thin filament disorganization and nemaline myopathy. *J. Clin. Invest.* **125**, 456–457 (2015).
17. E. Malfatti, J. Bohm, E. Lacene, M. Beuvin, N. B. Romero, J. Laporte, A premature stop codon in *MYO18B* is associated with severe nemaline myopathy with cardiomyopathy. *J. Neuromuscul. Dis.* **2**, 219–227 (2015).
18. G. Ravenscroft, S. Miyatake, V. L. Lehtokari, E. J. Todd, P. Vornanen, K. S. Yau, Y. K. Hayashi, N. Miyake, Y. Tsurusaki, H. Doi, H. Saitsu, H. Osaka, S. Yamashita, T. Ohya, Y. Sakamoto, E. Koshimizu, S. Imamura, M. Yamashita, K. Ogata, M. Shiina, R. J. Bryson-Richardson, R. Vaz, O. Ceyhan, C. A. Brownstein, L. C. Swanson, S. Monnot, N. B. Romero, H. Amthor, N. Kresoje, P. Sivadorai, C. Kiraly-Borri, G. Haliloglu, B. Talim, D. Orhan, G. Kale, A. K. Charles, V. A. Fabian, M. R. Davis, M. Lammens, C. A. Sewry, A. Manzur, F. Muntoni, N. F. Clarke, K. N. North, E. Bertini, Y. Nevo, E. Willichowski, I. E. Silberg, H. Topaloglu,

A. H. Beggs, R. J. Allcock, I. Nishino, C. Wallgren-Pettersson, N. Matsumoto, N. G. Laing, Mutations in KLHL40 are a frequent cause of severe autosomal-recessive nemaline myopathy. *Am. J. Hum. Genet.* **93**, 6–18 (2013).
19. N. Sambuughin, K. S. Yau, M. Olive, R. M. Duff, M. Bayarsaikhan, S. Lu, L. Gonzalez-Mera, P. Sivadorai, K. J. Nowak, G. Ravenscroft, F. L. Mastaglia, K. N. North, B. Ilkovski, H. Kremer, M. Lammens, B. G. van Engelen, V. Fabian, P. Lamont, M. R. Davis, N. G. Laing, L. G. Goldfarb, Dominant mutations in KBTBD13, a member of the BTB/Kelch family, cause nemaline myopathy with cores. *Am. J. Hum. Genet.* **87**, 842–847 (2010).
20. P. B. Agrawal, R. S. Greenleaf, K. K. Tomczak, V. L. Lehtokari, C. Wallgren-Pettersson, W. Wallefeld, N. G. Laing, B. T. Darras, S. K. Maciver, P. R. Dormitzer, A. H. Beggs, Nemaline myopathy with minicores caused by mutation of the CFL2 gene encoding the skeletal muscle actin-binding protein, cofilin-2. *Am. J. Hum. Genet.* **80**, 162–167 (2007).
21. K. Donner, M. Ollikainen, M. Ridanpaa, H.-J. Christen, H. H. Goebel, M. de Visser, K. Pelin, C. Wallgren-Pettersson, Mutations in the β-tropomyosin (TPM2) gene—A rare cause of nemaline myopathy. *Neuromuscul. Disord.* **12**, 151–158 (2002).
22. J. J. Johnston, R. I. Kelley, T. O. Crawford, D. H. Morton, R. Agarwala, T. Koch, A. A. Schaffer, C. A. Francomano, L. G. Biesecker, A novel nemaline myopathy in the Amish caused by a mutation in troponin T1. *Am. J. Hum. Genet.* **67**, 814–821 (2000).
23. K. Pelin, P. Hilpela, K. Donner, C. Sewry, P. A. Akkari, S. D. Wilton, D. Wattanasirichaigoon, M. L. Bang, T. Centner, F. Hanefeld, S. Odent, M. Fardeau, J. A. Urtizberea, F. Muntoni, V. Dubowitz, A. H. Beggs, N. G. Laing, S. Labeit, A. de la Chapelle, C. Wallgren-Pettersson, Mutations in the nebulin gene associated with autosomal recessive nemaline myopathy. *Proc. Natl. Acad. Sci. U.S.A.* **96**, 2305–2310 (1999).
24. K. J. Nowak, D. Wattanasirichaigoon, H. H. Goebel, M. Wilce, K. Pelin, K. Donner, R. L. Jacob, C. Hubner, K. Oexle, J. R. Anderson, C. M. Verity, K. N. North, S. T. Iannaccone, C. R. Muller, P. Nurnberg, F. Muntoni, C. Sewry, I. Hughes, R. Sutphen, A. G. Lacson, K. J. Swoboda, J. Vigneron, C. Wallgren-Pettersson, A. H. Beggs, N. G. Laing, Mutations in the skeletal muscle alpha-actin gene in patients with actin myopathy and nemaline myopathy. *Nat. Genet.* **23**, 208–212 (1999).
25. K. Pelin, M. Ridanpaa, K. Donner, S. Wilton, J. Krishnarajah, N. Laing, B. Kolmerer, S. Millevoi, S. Labeit, A. de la Chapelle, C. Wallgren-Petterson, Refined localisation of the genes for nebulin and titin on chromosome 2q allows the assignment of nebulin as a candidate gene for autosomal recessive nemaline myopathy. *Eur. J. Hum. Genet.* **5**, 229–234 (2019).
26. N. G. Laing, S. D. Wilton, P. A. Akkari, S. Dorosz, K. Boundy, C. Kneebone, P. Blumbergs, S. White, H. Watkins, D. R. Love, E. Haan, A mutation in the α tropomyosin gene *TPM3* associated with autosomal dominant nemaline myopathy NEM1. *Nat. Genet.* **10**, 249 (1995).
27. S. Miyatake, S. Mitsuhashi, Y. K. Hayashi, E. Purevjav, A. Nishikawa, E. Koshimizu, M. Suzuki, K. Yatabe, Y. Tanaka, K. Ogata, S. Kuru, M. Shiina, Y. Tsurusaki, M. Nakashima, T. Mizuguchi, N. Miyake, H. Saitsu, K. Ogata, M. Kawai, J. Towbin, I. Nonaka, I. Nishino, N. Matsumoto, Biallelic mutations in MYPN, encoding myopalladin, are associated with childhood-onset, slowly progressive nemaline myopathy. *Am. J. Hum. Genet.* **100**, 169–178 (2017).
28. M. Uhlén, L. Fagerberg, B. M. Hallström, C. Lindskog, P. Oksvold, A. Mardinoglu, Å. Sivertsson, C. Kampf, E. Sjöstedt, A. Asplund, I. M. Olsson, K. Edlund, E. Lundberg, S. Navani, C. A.-K. Szigyarto, J. Odeberg, D. Djureinovic, J. O. Takanen, S. Hober, T. Alm, P.-H. Edqvist, H. Berling, H. Tegel, J. Mulder, J. Rockberg, P. Nilsson, J. M. Schwenk, M. Hamsten, K. von Feilitzen, M. Forsberg, L. Persson, F. Johansson, M. Zwahlen, G. von Heijne, J. Nielsen, F. Pontén, Tissue-based map of the human proteome. *Science* **347**, 1260419 (2015).
29. J. M. de Winter, J. P. Molenaar, M. Yuen, R. van der Pijl, S. Shen, S. Conijn, M. van de Locht, M. Willigenburg, S. J. Bogaards, E. S. van Kleef, S. Lassche, M. Persson, D. E. Rassier, T. E. Sztal, A. A. Ruparelia, V. Oorschot, G. Ramm, T. E. Hall, Z. Xiong, C. N. Johnson, F. Li, B. Kiss, N. Lozano-Vidal, R. A. Boon, M. Marabita, L. Nogara, B. Blaauw, R. J. Rodenburg, B. Kusters, J. Doorduin, A. H. Beggs, H. Granzier, K. Campbell, W. Ma, T. Irving, E. Malfatti, N. B. Romero, R. J. Bryson-Richardson, B. G. van Engelen, N. C. Voermans, C. A. Ottenheijm, KBTBD13 is an actin-binding protein that modulates muscle kinetics. *J. Clin. Invest.* **130**, 754–767 (2020).
30. N. Sambuughin, W. Swietnicki, S. Techtmann, V. Matrosova, T. Wallace, L. Goldfarb, E. Maynard, KBTBD13 interacts with Cullin 3 to form a functional ubiquitin ligase. *Biochem. Biophys. Res. Commun.* **421**, 743–749 (2012).
31. J. P. Molenaar, E. van Kleef, E. van Zandvoort, N. van Alfen, B. G. van Engelen, N. C. Voermans, J. Doorduin, Detecting impaired muscle relaxation in myopathies with the use of motor cortical stimulation. *Neuromuscul. Disord.* **33**, 396–404 (2023).
32. I. M. Pauw-Gommans, K. H. Gerrits, A. de Haan, B. G. van Engelen, Muscle slowness in a family with nemaline myopathy. *Neuromuscul. Disord.* **16**, 477–480 (2006).
33. I. M. Gommans, B. G. van Engelen, H. J. ter Laak, H. G. Brunner, H. Kremer, M. Lammens, O. J. Vogels, A new phenotype of autosomal dominant nemaline myopathy. *Neuromuscul. Disord.* **12**, 13–18 (2002).
34. E. S. B. van Kleef, K. Bouman, J. P. F. Molenaar, B. Kusters, J. T. Groothuis, M. Olive, E. Malfatti, E. J. Kamsteeg, B. G. M. Van Engelen, C. A. C. Ottenheijm, J. Doorduin, N. C. Voermans, Nemaline myopathy type 6 caused by variants in the *KBTBD13* gene: A cross-sectional study of 24 patients. *Neurol. Genet.* **10**, e200214 (2024).
35. J. M. de Winter, K. Bouman, J. Strom, M. Methawasin, J. D. H. Jongbloed, W. van der Roest, J. V. Wijngaarden, J. Timmermans, R. Nijveldt, F. van den Heuvel, E. J. Kamsteeg, B. G. van Engelen, R. Galli, S. J. P. Bogaards, R. A. Boon, R. J. van der Pijl, H. Granzier, B. Koeleman, A. S. Amin, J. van der Velden, J. P. van Tintelen, M. P. van den Berg, K. Y. van Spaendonck-Zwarts, N. C. Voermans, C. A. C. Ottenheijm, KBTBD13 is a novel cardiomyopathy gene. *Hum. Mutat.* **43**, 1860–1865 (2022).
36. K. Bouman, B. Kusters, J. M. De Winter, C. Gillet, E. S. B. Van Kleef, L. Eshuis, G. Brochier, A. Madelaine, C. Labasse, C. Boulogne, B. G. M. Van Engelen, C. A. C. Ottenheijm, N. B. Romero, N. C. Voermans, E. Malfatti, NEM6, KBTBD13-related congenital myopathy: Myopathological analysis in 18 Dutch patients reveals ring rods fibers, cores, nuclear clumps, and granulo-filamentous protein material. *J. Neuropathol. Exp. Neurol.* **80**, 366–376 (2021).
37. I. M. Gommans, M. Davis, K. Saar, M. Lammens, F. Mastaglia, P. Lamont, G. van Duijnhoven, H. J. ter Laak, A. Reis, O. J. Vogels, N. Laing, B. G. van Engelen, H. Kremer, A locus on chromosome 15q for a dominantly inherited nemaline myopathy with core-like lesions. *Brain* **126**, 1545–1551 (2003).
38. M. Olive, L. G. Goldfarb, H. S. Lee, Z. Odgerel, A. Blokhin, L. Gonzalez-Mera, D. Moreno, N. G. Laing, N. Sambuughin, Nemaline myopathy type 6: Clinical and myopathological features. *Muscle Nerve* **42**, 901–907 (2010).
39. N. C. Voermans, A. Ferreiro, A. Aartsema-Rus, H. Jungbluth, Gene therapy for X-linked myotubular myopathy: The challenges. *Lancet Neurol.* **22**, 1089–1091 (2023).
40. M. Yamaguchi, R. M. Robson, M. H. Stromer, D. S. Dahl, T. Oda, Nemaline myopathy rod bodies. Structure and composition. *J. Neurol. Sci.* **56**, 35–56 (1982).
41. A. Vandebrouck, A. Domazetovska, N. Mokbel, S. T. Cooper, B. Ilkovski, K. N. North, In vitro analysis of rod composition and actin dynamics in inherited myopathies. *J. Neuropathol. Exp. Neurol.* **69**, 429–441 (2010).
42. B. Kiss, E. J. Lee, W. Ma, F. W. Li, P. Tonino, S. M. Mijailovich, T. C. Irving, H. L. Granzier, Nebulin stiffens the thin filament and augments cross-bridge interaction in skeletal muscle. *Proc. Natl. Acad. Sci. U.S.A.* **115**, 10369–10374 (2018).
43. A. M. Abdelmoez, L. Sardon Puig, J. A. B. Smith, B. M. Gabriel, M. Savikj, L. Dollet, A. V. Chibalin, A. Krook, J. R. Zierath, N. J. Pillon, Comparative profiling of skeletal muscle models reveals heterogeneity of transcriptome and metabolism. *Am. J. Physiol. Cell Physiol.* **318**, C615–C626 (2020).
44. A. T. Kho, P. B. Kang, I. S. Kohane, L. M. Kunkel, Transcriptome-scale similarities between mouse and human skeletal muscles with normal and myopathic phenotypes. *BMC Musculoskelet. Disord.* **7**, 23 (2006).
45. Z. Xie, A. Bailey, M. V. Kuleshov, D. J. B. Clarke, J. E. Evangelista, S. L. Jenkins, A. Lachmann, M. L. Wojciechowicz, E. Kropiwnicki, K. M. Jagodnik, M. Jeon, A. Ma'ayan, Gene set knowledge discovery with Enrichr. *Curr. Protoc.* **1**, e90 (2021).
46. M. V. Kuleshov, M. R. Jones, A. D. Rouillard, N. F. Fernandez, Q. Duan, Z. Wang, S. Koplev, S. L. Jenkins, K. M. Jagodnik, A. Lachmann, M. G. McDermott, C. D. Monteiro, G. W. Gundersen, A. Ma'ayan, Enrichr: A comprehensive gene set enrichment analysis web server 2016 update. *Nucleic Acids Res.* **44**, W90–W97 (2016).
47. E. Y. Chen, C. M. Tan, Y. Kou, Q. Duan, Z. Wang, G. V. Meirelles, N. R. Clark, A. Ma'ayan, Enrichr: Interactive and collaborative HTML5 gene list enrichment analysis tool. *BMC Bioinformatics* **14**, 128 (2013).
48. M. A. Nguyen, J. E. Joya, A. J. Kee, A. Domazetovska, N. Yang, J. W. Hook, F. A. Lemckert, E. Kettle, V. A. Valova, P. J. Robinson, K. N. North, P. W. Gunning, C. A. Mitchell, E. C. Hardeman, Hypertrophy and dietary tyrosine ameliorate the phenotypes of a mouse model of severe nemaline myopathy. *Brain* **134**, 3516–3529 (2011).
49. J. Lindqvist, E. J. Lee, E. Karimi, J. Kolb, H. Granzier, Omecamtiv mecarbil lowers the contractile deficit in a mouse model of nebulin-based nemaline myopathy. *PLOS ONE* **14**, e0224467 (2019).
50. F. Li, J. Kolb, J. Crudele, P. Tonino, Z. Hourani, J. E. Smith III, J. S. Chamberlain, H. Granzier, Expressing a Z-disk nebulin fragment in nebulin-deficient mouse muscle: Effects on muscle structure and function. *Skelet. Muscle* **10**, 2 (2020).
51. O. E. Karpicheva, S. V. Avrova, A. L. Bogdanov, V. V. Sirenko, C. S. Redwood, Y. S. Borovikov, Molecular mechanisms of deregulation of muscle contractility caused by the R168H mutation in TPM3 and its attenuation by therapeutic agents. *Int. J. Mol. Sci.* **24**, 5829 (2023).
52. E. J. Lee, J. Kolb, D. T. Hwee, F. I. Malik, H. L. Granzier, Functional characterization of the intact diaphragm in a nebulin-based nemaline myopathy (NM) model-effects of the fast skeletal muscle troponin activator tirasemtiv. *Int. J. Mol. Sci.* **20**, 5008 (2019).
53. J. M. de Winter, C. Gineste, E. Minardi, L. Brocca, M. Rossi, T. Borsboom, A. H. Beggs, M. Bernard, D. Bendahan, D. T. Hwee, F. I. Malik, M. A. Pellegrino, R. Bottinelli, J. Gondin, C. A. C. Ottenheijm, Acute and chronic tirasemtiv treatment improves in vivo and in vitro muscle performance in actin-based nemaline myopathy mice. *Hum. Mol. Genet.* **30**, 1305–1320 (2021).
54. T. E. Sztal, E. A. McKaige, C. Williams, V. Oorschot, G. Ramm, R. J. Bryson-Richardson, Testing of therapies in a novel nebulin nemaline myopathy model demonstrate a lack of efficacy. *Acta Neuropathol. Commun.* **6**, 40 (2018).
55. R. A. Galli, T. C. Borsboom, C. Gineste, L. Brocca, M. Rossi, D. T. Hwee, F. I. Malik, R. Bottinelli, J. Gondin, M. A. Pellegrino, J. M. de Winter, C. A. C. Ottenheijm, Tirasemtiv enhances

submaximal muscle tension in an Acta1:p.Asp286Gly mouse model of nemaline myopathy. *J. Gen. Physiol.* **156**, e202313471 (2024).
56. M. M. Ryan, B. Ilkovski, C. D. Strickland, C. Schnell, D. Sanoudou, C. Midgett, R. Houston, D. Muirhead, X. Dennett, L. K. Shield, U. De Girolami, S. T. Iannaccone, N. G. Laing, K. N. North, A. H. Beggs, Clinical course correlates poorly with muscle pathology in nemaline myopathy. *Neurology* **60**, 665–673 (2003).
57. J. E. Joya, A. J. Kee, V. Nair-Shalliker, M. Ghoddusi, M. A. Nguyen, P. Luther, E. C. Hardeman, Muscle weakness in a mouse model of nemaline myopathy can be reversed with exercise and reveals a novel myofiber repair mechanism. *Hum. Mol. Genet.* **13**, 2633–2645 (2004).
58. S. Schiaffino, C. Reggiani, Fiber types in mammalian skeletal muscles. *Physiol. Rev.* **91**, 1447–1531 (2011).
59. M. A. Pellegrino, M. Canepari, R. Rossi, G. D'Antona, C. Reggiani, R. Bottinelli, Orthologous myosin isoforms and scaling of shortening velocity with body size in mouse, rat, rabbit and human muscles. *J. Physiol.* **546**, 677–689 (2003).
60. G. Gouspillou, N. Sgarioto, B. Norris, S. Barbat-Artigas, M. Aubertin-Leheudre, J. A. Morais, Y. Burelle, T. Taivassalo, R. T. Hepple, The relationship between muscle fiber type-specific PGC-1α content and mitochondrial content varies between rodent models and humans. *PLOS ONE* **9**, e103044 (2014).
61. F. Rudolph, J. Huttemeister, K. da Silva Lopes, R. Juttner, L. Yu, N. Bergmann, D. Friedrich, S. Preibisch, E. Wagner, S. E. Lehnart, C. C. Gregorio, M. Gotthardt, Resolving titin's lifecycle and the spatial organization of protein turnover in mouse cardiomyocytes. *Proc. Natl. Acad. Sci. U.S.A.* **116**, 25126–25136 (2019).
62. Y. Kitajima, Y. Tashiro, N. Suzuki, H. Warita, M. Kato, M. Tateyama, R. Ando, R. Izumi, M. Yamazaki, M. Abe, K. Sakimura, H. Ito, M. Urushitani, R. Nagatomi, R. Takahashi, M. Aoki, Proteasome dysfunction induces muscle growth defects and protein aggregation. *J. Cell Sci.* **127**, 5204–5217 (2014).
63. C. Gineste, A. Simon, M. Braun, D. Reiss, J. Laporte, Tamoxifen improves muscle structure and function of Bin1- and Dnm2-related centronuclear myopathies. *Brain* **146**, 3029–3048 (2023).
64. D. Sellung, L. Heil, N. Daya, F. Jacobsen, J. Mertens-Rill, H. Zhuge, K. Doring, M. Piran, H. Milting, A. Unger, W. A. Linke, R. Kley, C. Preusse, A. Roos, D. O. Furst, P. Ven, M. Vorgerd, Novel filamin C myofibrillar myopathy variants cause different pathomechanisms and alterations in protein quality systems. *Cells* **12**, 1321 (2023).
65. A. C. Nascimbeni, M. Fanin, E. Masiero, C. Angelini, M. Sandri, Impaired autophagy contributes to muscle atrophy in glycogen storage disease type II patients. *Autophagy* **8**, 1697–1700 (2012).
66. P. Grumati, L. Coletto, P. Sabatelli, M. Cescon, A. Angelin, E. Bertaggia, B. Blaauw, A. Urciuolo, T. Tiepolo, L. Merlini, N. M. Maraldi, P. Bernardi, M. Sandri, P. Bonaldo, Autophagy is defective in collagen VI muscular dystrophies, and its reactivation rescues myofiber degeneration. *Nat. Med.* **16**, 1313–1320 (2010).
67. A.-C. Durieux, S. Vassilopoulos, J. Lainé, B. Fraysse, L. Briñas, B. Prudhon, J. Castells, D. Freyssenet, G. Bonne, P. Guicheney, M. Bitoun, A centronuclear myopathy–dynamin 2 mutation impairs autophagy in mice. *Traffic* **13**, 869–879 (2012).
68. A. A. Ruparelia, V. Oorschot, G. Ramm, R. J. Bryson-Richardson, FLNC myofibrillar myopathy results from impaired autophagy and protein insufficiency. *Hum. Mol. Genet.* **25**, 2131–2142 (2016).
69. D. C. Rubinsztein, G. Marino, G. Kroemer, Autophagy and aging. *Cell* **146**, 682–695 (2011).
70. L. Buscara, D. A. Gross, N. Daniele, Of rAAV and men: From genetic neuromuscular disorder efficacy and toxicity preclinical studies to clinical trials and back. *J. Pers. Med.* **10**, 258 (2020).
71. L. Servais, R. Horton, D. Saade, C. Bonnemann, F. Muntoni, 261st ENMC Workshop Study Group, 261st ENMC International Workshop: Management of safety issues arising following AAV gene therapy. 17th–19th June 2022, Hoofddorp, Netherlands. *Neuromuscul. Disord.* **33**, 884–896 (2023).
72. J. Weinmann, S. Weis, J. Sippel, W. Tulalamba, A. Remes, J. El Andari, A. K. Herrmann, Q. H. Pham, C. Borowski, S. Hille, T. Schonberger, N. Frey, M. Lenter, T. VandenDriessche, O. J. Muller, M. K. Chuah, T. Lamla, D. Grimm, Identification of a myotropic AAV by massively parallel in vivo evaluation of barcoded capsid variants. *Nat. Commun.* **11**, 5432 (2020).
73. M. Tabebordbar, K. A. Lagerborg, A. Stanton, E. M. King, S. Ye, L. Tellez, A. Krunnfusz, S. Tavakoli, J. J. Widrick, K. A. Messemer, E. C. Troiano, B. Moghadaszadeh, B. L. Peacker, K. A. Leacock, N. Horwitz, A. H. Beggs, A. J. Wagers, P. C. Sabeti, Directed evolution of a family of AAV capsid variants enabling potent muscle-directed gene delivery across species. *Cell* **184**, 4919–4938.e22 (2021).
74. J. El Andari, E. Renaud-Gabardos, W. Tulalamba, J. Weinmann, L. Mangin, Q. H. Pham, S. Hille, A. Bennett, E. Attebi, E. Bourges, C. Leborgne, N. Guerchet, J. Fakhiri, C. Kramer, E. Wiedtke, R. McKenna, L. Guianvarc'h, M. Toueille, G. Ronzitti, M. Hebben, F. Mingozzi, T. VandenDriessche, M. Agbandje-McKenna, O. J. Muller, M. K. Chuah, A. Buj-Bello, D. Grimm, Semirational bioengineering of AAV vectors with increased potency and specificity for systemic gene therapy of muscle disorders. *Sci. Adv.* **8**, eabn4704 (2022).
75. Y. Perez-Riverol, C. Bandla, D. J. Kundu, S. Kamatchinathan, J. Bai, S. Hewapathirana, N. S. John, A. Prakash, M. Walzer, S. Wang, J. A. Vizcaino, The PRIDE database at 20 years: 2025 update. *Nucleic Acids Res.* **53**, D543–D553 (2025).
76. C. A. Schneider, W. S. Rasband, K. W. Eliceiri, NIH Image to ImageJ: 25 years of image analysis. *Nat. Methods* **9**, 671–675 (2012).
77. K. J. Livak, T. D. Schmittgen, Analysis of relative gene expression data using real-time quantitative PCR and the $2^{-\Delta\Delta CT}$ method. *Methods* **25**, 402–408 (2001).
78. R. Fischetti, S. Stepanov, G. Rosenbaum, R. Barrea, E. Black, D. Gore, R. Heurich, E. Kondrashkina, A. J. Kropf, S. Wang, K. Zhang, T. C. Irving, G. B. Bunker, The BioCAT undulator beamline 18ID: A facility for biological non-crystalline diffraction and X-ray absorption spectroscopy at the Advanced Photon Source. *J. Synchrotron Radiat.* **11**, 399–405 (2004).
79. T. C. Irving, B. M. Millman, Changes in thick filament structure during compression of the filament lattice in relaxed frog sartorius muscle. *J. Muscle Res. Cell Motil.* **10**, 385–394 (1989).
80. K. Wakabayashi, Y. Sugimoto, H. Tanaka, Y. Ueno, Y. Takezawa, Y. Amemiya, X-ray diffraction evidence for the extensibility of actin and myosin filaments during muscle contraction. *Biophys. J.* **67**, 2422–2435 (1994).
81. J. Jiratrakanvong, J. Shao, J. Li, M. Menendez Alvarez, X. Li, P. Das, G. Nikseresht, N. Miskin, R. Huo, J. Nabon, T. Leduc, E. Zhang, W. Ma, G. Agam, T. C. Irving, MuscleX: Data analysis software for fiber diffraction patterns from muscle. *J. Synchrotron Radiat.* **31**, 1401–1408 (2024).
82. A. Frankish, S. Carbonell-Sala, M. Diekhans, I. Jungreis, J. E. Loveland, J. M. Mudge, C. Sisu, J. C. Wright, C. Arnan, I. Barnes, A. Banerjee, R. Bennett, A. Berry, A. Bignell, C. Boix, F. Calvet, D. Cerdan-Velez, F. Cunningham, C. Davidson, S. Donaldson, C. Dursun, R. Fatima, S. Giorgetti, C. G. Giron, J. M. Gonzalez, M. Hardy, P. W. Harrison, T. Hourlier, Z. Hollis, T. Hunt, B. James, Y. Jiang, R. Johnson, M. Kay, J. Lagarde, F. J. Martin, L. M. Gomez, S. Nair, P. Ni, F. Pozo, V. Ramalingam, M. Ruffier, B. M. Schmitt, J. M. Schreiber, E. Steed, M. M. Suner, D. Sumathipala, I. Sycheva, B. Uszczynska-Ratajczak, E. Wass, Y. T. Yang, A. Yates, Z. Zafrulla, J. S. Choudhary, M. Gerstein, R. Guigo, T. J. P. Hubbard, M. Kellis, A. Kundaje, B. Paten, M. L. Tress, P. Flicek, GENCODE: Reference annotation for the human and mouse genomes in 2023. *Nucleic Acids Res.* **51**, D942–D949 (2023).
83. A. Dobin, C. A. Davis, F. Schlesinger, J. Drenkow, C. Zaleski, S. Jha, P. Batut, M. Chaisson, T. R. Gingeras, STAR: Ultrafast universal RNA-seq aligner. *Bioinformatics* **29**, 15–21 (2013).
84. S. Anders, P. T. Pyl, W. Huber, HTSeq—A Python framework to work with high-throughput sequencing data. *Bioinformatics* **31**, 166–169 (2015).
85. M. I. Love, W. Huber, S. Anders, Moderated estimation of fold change and dispersion for RNA-seq data with DESeq2. *Genome Biol.* **15**, 550 (2014).
86. S. Sayols, D. Scherzinger, H. Klein, dupRadar: A Bioconductor package for the assessment of PCR artifacts in RNA-Seq data. *BMC Bioinformatics* **17**, 428 (2016).
87. A. M. Bolger, M. Lohse, B. Usadel, Trimmomatic: A flexible trimmer for Illumina sequence data. *Bioinformatics* **30**, 2114–2120 (2014).
88. D. Kim, B. Langmead, S. L. Salzberg, HISAT: A fast spliced aligner with low memory requirements. *Nat. Methods* **12**, 357–360 (2015).
89. M. D. Robinson, D. J. McCarthy, G. K. Smyth, edgeR: A Bioconductor package for differential expression analysis of digital gene expression data. *Bioinformatics* **26**, 139–140 (2010).
90. M. E. Ritchie, B. Phipson, D. Wu, Y. Hu, C. W. Law, W. Shi, G. K. Smyth, limma powers differential expression analyses for RNA-sequencing and microarray studies. *Nucleic Acids Res.* **43**, e47 (2015).
91. C. W. Law, Y. Chen, W. Shi, G. K. Smyth, voom: Precision weights unlock linear model analysis tools for RNA-seq read counts. *Genome Biol.* **15**, R29 (2014).
92. B. V. Schomakers, A. S. Passadouro, M. M. Tretowicz, P. J. Simpson, Y. R. J. Jaspers, M. van Weeghel, I. M. Hu, C. M. E. Lamboo, D. Cloutier, B. J. Byrne, J. B. van Klinken, P. M. L. Janssen, S. R. Piersma, C. R. Jimenez, F. M. Vaz, G. S. Salomons, J. van der Velden, R. H. Houtkooper, S. Mosegaard, Integrated multi-omics mapping of mitochondrial dysfunction and substrate preference in Barth syndrome cardiac tissue. *EMBO Mol. Med.* **17**, 3227–3246 (2025).

Acknowledgments: We thank M. Mol, S. Meijer, Y. Meijer, J. Hollander, A. Varma, M. van Vliet, and R. Baelsar for technical support. **Funding:** This study was funded by a ZonMW-VICI grant (number 91819613 to C.A.C.O), Prinses Beatrix Spierfonds and A Foundation Building Strength (grant number W.OR23-06 to C.A.C.O.), and a ZonMW VENI grant (number 09150161910168 to J.M.d.W.) and used resources of the Advanced Photon Source, a US Department of Energy (DOE) Office of Science User Facility, operated for the DOE Office of Science by Argonne National Laboratory under contract no. DE-AC02-06CH11357. BioCAT was supported by the National Institute of General Medical Sciences of the National Institutes of Health (grant P30 GM138395 to T.I.). **Author contributions:** R.A.G., C.A.C.O., and J.M.d.W. conceived, designed, and supervised the study. R.A.G., N.V., B.v.E., and K.B. performed the human histological studies. R.A.G. and E.S. conducted the natural history contractile and morphological characterization experiments. R.A.G., S.C., S.B., T.J.K., L.A.V., and H.G. performed the protein

polymerization and in vitro/in vivo recombinant protein localization assays. X-ray diffraction studies were carried out by R.A.G., S.C., W.M., and T.I. Bulk RNA sequencing and myofiber-specific RNA sequencing analyses were performed by R.A.G., A.v.d.H., S.M.v.d.M., R.J.B., J.M.d.W., and C.A.C.O. Proteomic studies and intramuscular knockdown experiments were conducted by R.A.G. and R.J.B. R.A.G. performed the knockdown contractile and morphological characterization studies. O.A. designed the knockdown constructs. L.A.V. conducted the knockdown mouse model characterization studies. Visualization and figure preparation were performed by R.A.G. R.A.G. drafted the original manuscript. All authors contributed to data interpretation and manuscript review and editing and approved the final version of the manuscript. **Competing interests:** The authors declare that they have no competing interests. **Data, code, and materials availability:** All data associated with this study are present in the paper or the Supplementary Materials. The mass spectrometry proteomic data have been deposited in the ProteomeXchange Consortium via PRIDE (*75*) partner repository with the dataset identifier PXD071917 and DOI 10.6019/PXD071917. The mouse soleus bulk and fiber type–specific RNA sequencing data have been deposited to Gene Expression Omnibus (GEO) under accession number GSE322917, and the human fiber type–specific RNA sequencing data have been deposited to the European Genome-Phenome Archive (EGA) with data identifier number EGAC0000000923. All sequencing data were analyzed using standard R packages, and no code was generated for this study. For a detailed description of the data analysis, see Materials and Methods. All materials used or generated in this study are commercially available or will be supplied upon reasonable request to the corresponding authors.

Submitted 20 March 2025
Resubmitted 19 December 2025
Accepted 4 June 2026
Published 24 June 2026
10.1126/scitranslmed.adx2116

Science Translational Medicine

Kbtbd13 knockdown restores muscle function in a clinically relevant mouse model of nemaline myopathy type 6

Ricardo A. Galli, Leander A. Vonk, Rianne J. Baelde, Anita van den Heuvel, Sylvia Bogaards, Stefan Conijn, Emma Siteur, Olga Alekhina, Henk Granzier, Thomas Irving, Weikang Ma, Karlijn Bouman, Baziel van Engelen, Silvère M. van der Maarel, Tyler J. Kirby, Nicol Voermans, Josine de Winter, and Coen A.C. Ottenheijm

Sci. Transl. Med. **18** (855), eadx2116. DOI: 10.1126/scitranslmed.adx2116

Editor's summary

Nemaline myopathy type 6 (NEM6) is a nondystrophic congenital myopathy caused by pathogenic variants in the gene *Kelch repeat and BTB domain–containing 13* (*KBTBD13*) and is characterized by muscle weakness and impaired muscle relaxation kinetics for which there is no current treatment. Here, Galli and colleagues characterized the *Kbtbd13*:p.Arg408Cys mouse knockin model, which carries the Dutch gain-of-function founder variant, and compared it with patient samples to provide deeper insights into the disease. Treating 3-month-old knockin mice with intramuscular short hairpin RNA therapy after phenotype onset restored normal myofiber-type distribution, cleared nemaline rods, and improved muscle relaxation kinetics by 9 months of age, suggesting the potential benefit of *KBTBD13*-targeted strategies for patients with NEM6. —Melissa L. Norton